Chapter 5

The Crab Pulsar and Nebula

The Crab complex is one of the most studied objects in all of astronomy. As the brightest supernova remnant in the sky, the Crab nebula has been the focus of observations for centuries. Indeed, the conclusion that it is a Type II supernova which appeared on July 4, 1054 A.D is based on the recorded observations of early Far Eastern and Native American astronomers. The Crab nebula has been confirmed as a center-filled supernova remnant, and has been detected at radio, optical, and X-ray wavelengths (see Mitton 1978 for a full review). Even before the discovery of pulsars, Hoyle, Narlikar, & Wheeler (1964) suggested that a neutron star with a strong magnetic field might exist at the center of the nebula, and Pacini (1967) theorized that a rapidly rotating, highly magnetized neutron star could be powering the entire Crab nebula. When the Crab pulsar (PSR B0531+21) was detected at the center of the nebula (Staelin & Reifenstein 1968), it was soon clear that it was unique among the radio pulsars. With a period of 33.4 ms, it was the fastest pulsar known for many years; it was the first pulsar confirmed to be decelerating (Richards & Comella 1969); it has the youngest characteristic age and highest rotational energy loss rate of the known radio pulsars (Taylor, Manchester & Lyne 1993); and it was the first pulsar to be detected at optical, X-ray, and γ-ray wavelengths (Cocke, Disney, & Taylor 1969; Fritz et al. 1969; Bradt et al. 1969; Browning, Ramsden, & Wright 1971; Albats et al. 1972; Kinzer, Share, & Seeman 1973; McBreen et al. 1973; Parlier et al. 1973). The Crab complex is also noteworthy in that it was one of the first point-like objects to be detected at GeV and TeV energies (Kniffen et al. 1974; Akerlof et al. 1989; Weekes et al. 1989).

Since the nebular contribution to the luminosity of the Crab dominates the pulsed component at lower energies, it is possible that there might be an unpulsed nebular component in the detected γ-radiation as well. The nebular emission spectrum is well fit from X-ray to MeV energies by a single power law with index -2.08 (Toor & Seward 1974; Walraven et al. 1975), consistent with a primary emission mechanism of synchrotron radiation. Extrapolation of the power law implies that a significant amount of unpulsed radiation from the Crab will be emitted in the *EGRET* observational energy range. Unlike detectors at lower energies, however, current γ-ray telescopes do not have sufficient angular resolution to separate the pulsar radiation from any possible nebular emission. Nevertheless, previous high-energy γ-ray observations of the Crab complex by *SAS 2* and *COS B* (Thompson et al. 1977; Bennett et al. 1977b; Clear et al. 1987) have revealed that the total emission above 100 MeV is almost entirely pulsed. The increased statistics achieved by *EGRET* provide a better opportunity to determine the extent of any unpulsed emission, as well as its spectral behavior.

Even though the Crab pulsar signal is engulfed by the surrounding nebular emission at radio frequencies, individual pulses can still be detected by radio observatories due to the unique property that the Crab pulsar displays in emitting *giant pulses* (Heiles, Campbell, & Rankin 1970; Staelin & Sutton 1970). While other radio pulsars have exponential or Gaussian individual pulse flux density distributions with a maximum intensity of about 10 times the average (Hesse & Wielebinski 1974; Ritchings 1976), a single giant pulse from the Crab pulsar can be as much as 2000 times the average pulse flux density amplitude (Lundgren et al. 1995). This phenomenon is observed in both of the main radio pulses, but not in the precursor which appears at radio frequencies below 600 MHz (Gower & Argyle; Argyle 1973). Considering that the Crab pulse profile has consistent shape from radio to γ-ray energies (see Figure 2.1), the multiwavelength emission corresponding to each peak must be coming from essentially the same region in the magnetosphere, so it is reasonable to expect that there might be some correlation between the occurrence of a giant pulse at radio frequencies and enhanced γ-ray emission. This possibility has been explored through a cooperative effort between *CGRO* instruments and radio astronomers, and the *EGRET* results are presented in §5.6.

In this chapter, a detailed analysis of the Crab pulsar and nebula using the first three phases of *EGRET* observations is presented. A similar study using only the first two months of observations was originally presented by Nolan et al. (1993).

5.1 Spatial Analysis

The Crab region was within 25° of the instrument pointing axis during the 15 observations listed in Table 5.1. The pointing direction, source aspect angle from the instrument pointing axis, and net instrument exposure above 100 MeV are listed for each observation. The total exposure for the 15 observations is 1.8×10^9 cm^2 s, which is more than an order of magnitude

Table 5.1: *EGRET* Observations of the Crab Region

Viewing Period	Observation Dates	Pointing Axis (J2000)		Aspect Angle	Exposure (> 100 MeV) (10^7 cm^2 s)
		RA	DEC		
0002	1991 Apr 22–28	86°.76	22°.09	2°.9	17.8
0003	1991 Apr 28–May 1	89.80	15.25	8.9	9.3
0004	1991 May 1–4	89.77	15.24	8.9	9.0
0005	1991 May 4–7	83.52	22.02	0.1	11.7
0010	1991 May 16–30	88.07	17.14	6.4	40.8
0021	1991 June 8–15	87.83	12.47	10.4	14.4*
0360	1992 Aug 11–12	68.98	30.42	15.6	1.8
0365	1992 Aug 12–20	69.39	32.90	16.7	7.4
0390	1992 Sep 1–17	68.87	33.82	17.6	12.4
2130	1993 Mar 23–29	80.30	22.29	3.1	5.8
2210	1993 May 13–24	85.21	19.46	2.9	10.4
3100	1993 Dec 1–13	98.48	17.77	14.6	9.2
3211	1994 Feb 8–15	84.73	26.32	4.4	14.2
3215	1994 Feb 15–17	84.73	26.32	4.4	4.7
3370	1994 Aug 9–29	87.70	0.98	21.4	12.4

* Excludes ~8.5 hour time period of solar flare on 1991 June 11.

greater exposure than was obtained by *COS B* during its ~7 year lifetime (Clear et al. 1987). Most of the *EGRET* exposure occurred during Phase I of the *CGRO* mission. Analysis of the Crab complex is complicated by the fact that the only solar flare detected by *EGRET* occurred on 1991 June 11 (Kanbach et al. 1993), when the Sun was in a direction only ~ 4°.4 from that of the Crab pulsar. Even though γ-ray emission from the flare lasted only ~8.5 hours, its γ-ray flux level above 100 MeV over that time period exceeded the Crab flux level by more than an order of magnitude. While *EGRET* has sufficient angular resolution above 100 MeV to distinguish the two sources, below 100 MeV the instrument PSF becomes rather broad, and a high degree of source confusion arises between Crab and the soft spectrum solar flare. Rather than introduce possible errors by trying to account for the solar flare emission, the studies in this chapter exclude data from the ~8.5 hour flare period during VP 0021.

Likelihood analysis on the combined spatial maps of the viewing periods listed in Table 5.1 reveals that there is a point source consistent with the Crab radio pulsar position, measuring a flux of $(2.39 \pm 0.05) \times 10^{-6}$ photons cm^{-2} s^{-1} above 100 MeV. The maximum TS position falls at $l = 184\overset{\circ}{.}53$, $b = -5\overset{\circ}{.}83$, which is $\sim 3'$ from the radio pulsar position. The confidence contours for the Crab are shown in Figure 5.1. The radio position of the

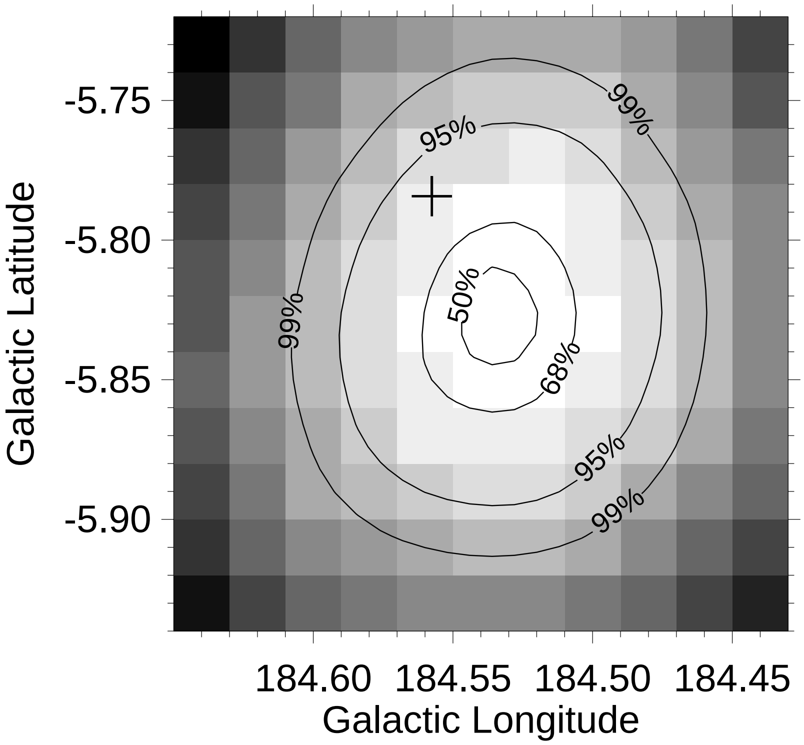

Figure 5.1: Spatial confidence contours for the Crab region above 100 MeV. The contours are derived from a map of the likelihood test statistic TS. The cross indicates the radio position of the Crab pulsar.

Crab pulsar falls within the 95% contour.

The Crab is detectable as a compact γ-ray point source over each of the ten standard energy ranges from 30 MeV–10 GeV, enabling its spectral behavior to be studied over an extended energy range. Likelihood analysis is not performed above 10 GeV because the correspondingly low photon statistics make it difficult to perform effective maximum likelihood parameter estimation. The differential photon spectrum from 30 MeV to 10 GeV is plotted in Figure 5.2. As with all plots in this thesis, the error bars represent the 1σ uncertainty levels. This plot shows that the total Crab emission generally behaves as a power law over the energy range 100 MeV–10 GeV with a functional form

$$\frac{dN}{dE} = (2.56 \pm 0.06) \times 10^{-9} \left(\frac{E}{299\ \mathrm{MeV}}\right)^{-2.12\pm0.03} \ \mathrm{photons\ cm^{-2}\ s^{-1}\ MeV^{-1}}\ , \qquad (5.1)$$

where the energy normalization factor of 299 MeV has been chosen so that the errors in the overall normalization and spectral index will be uncorrelated. A spectral fit should be performed only over the energy range where the emission behaves as a simple power law.

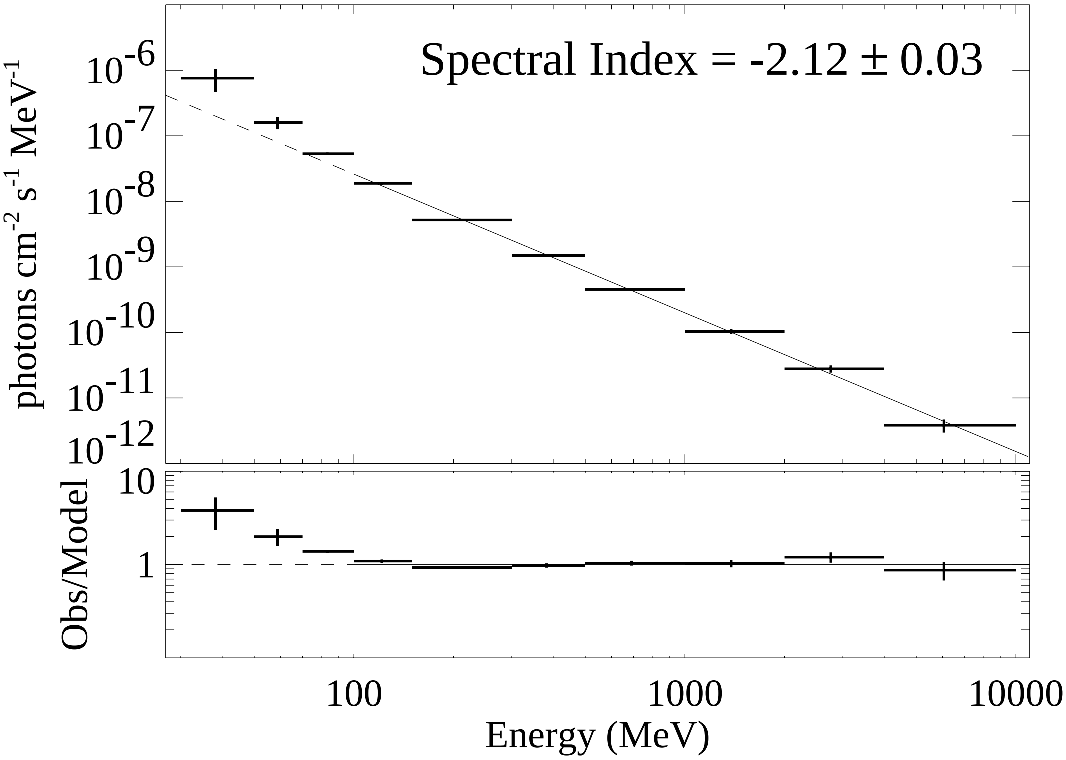

Figure 5.2: Differential photon spectrum of the total emission from Crab derived using spatial analysis. The upper panel shows the power law fit, while the lower panel plots the observed values divided by the values predicted from the power law fit. The fit is to the data points between 100 MeV and 10 GeV, with the dashed line indicating the extrapolated power law down to 30 MeV.

Therefore, the first three bins from 30–100 MeV are not included in the fit, as they deviate significantly from the trend established by the higher energy bins. This is particularly evident in the lower panel of Figure 5.2 which plots the measured flux divided by the values predicted by equation (5.1). The deviation at low energies suggests that the Crab total spectrum is much softer for $E < 100$ MeV. For the fit shown in Figure 5.2, the χ^2 test statistic defined in equation (4.49) is 10.7 with 5 degrees of freedom (DOF), which suggests a probability of 5.9% that the measured flux values could be drawn from the power law given by equation (5.1). If all ten bins are included in the spectral fit, the derived spectral index of -2.20 ± 0.02 agrees with the results derived from *COS B* observations of the Crab region (Hermsen 1980), but the χ^2 test statistic is 47.5 with 8 DOF, implying that the probability that the 10 measured values are drawn from a photon spectrum behaving as a simple power law over the entire *EGRET* energy range is 1.2×10^{-7}.

In most observational wavelengths, the Crab has been found to be a very stable emitter

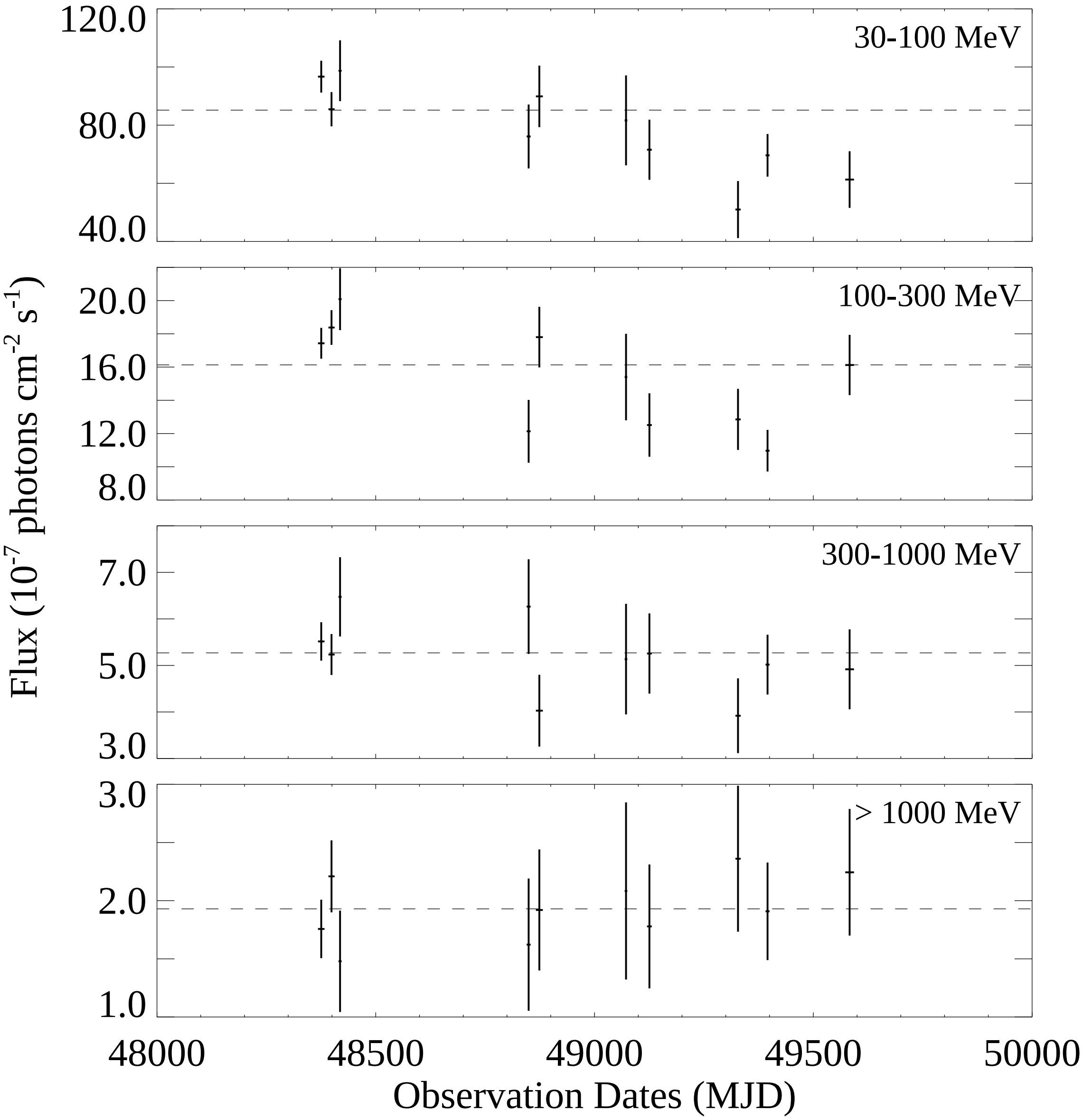

Figure 5.3: Temporal variation of the total Crab γ-ray intensity over four independent energy ranges. The dashed line in each plot indicates the average value determined from the summation of all of the observations. The observation dates are plotted in units of Modified Julian Days (MJD).

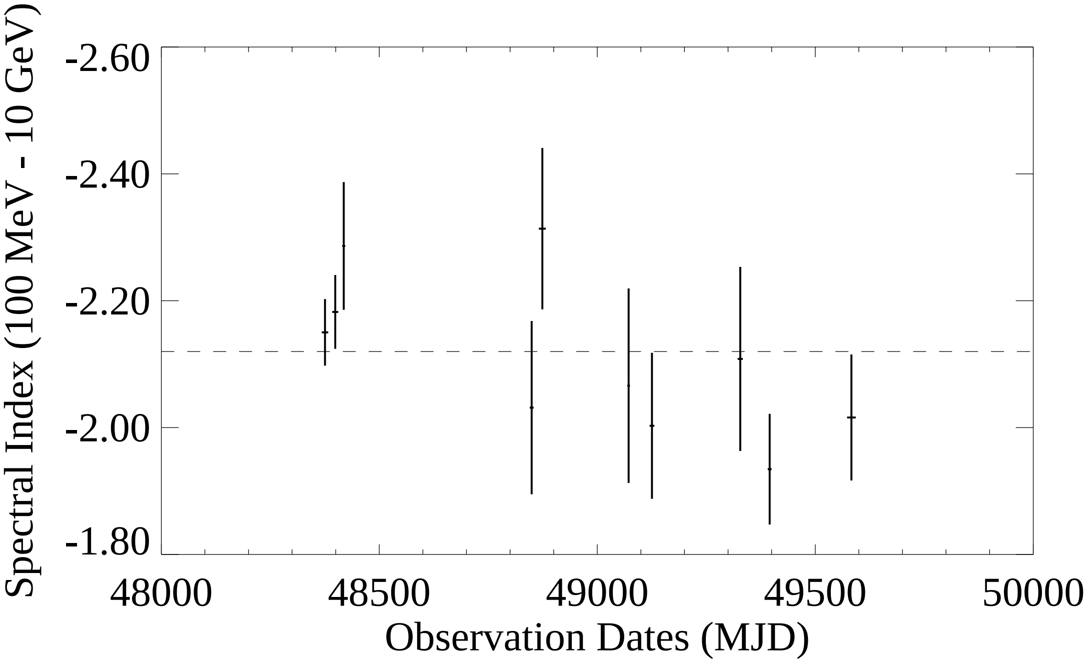

Figure 5.4: Temporal variation of the differential photon spectral index for the total Crab γ-ray emission. For each observation, the fit was performed over the energy range 100 MeV–10 GeV. The dashed line indicates the value determined from the summation of all of the observations.

and is often used as a calibration source. As a test of whether the Crab behaves as a steady point-like source in the *EGRET* observational energy range, the total flux and spectral index are determined for each observation in Table 5.1. To improve the statistics, the consecutive observations VP 0002, 0003, 0004, and 0005 are treated as a single observation. Likewise, VP 0360 is combined with VP 0365, and VP 3211 is added to VP 3215. The total flux measured in each observation is plotted for four independent energy ranges in Figure 5.3, and the corresponding spectral indices determined for the energy range 100 MeV–10 GeV are shown in Figure 5.4. The two lower energies, 30–100 MeV and 100-300 MeV, show significant evidence of variation, measuring high χ^2 values of 29.2 and 40.0 for 9 degrees of freedom. Furthermore, it is clear that the level of flux measured in the 30-100 MeV energy range is decreasing with time. This appears to indicate that the the energy-dependent correction factors discussed in §3.4 do not fully correct for the *EGRET* loss in sensitivity at low energies as the instrument ages. As will be shown in §12.1.4, the residual instrumental drift is small, and the apparent variability is not very significant when the systematic uncertainties of order ~5% are taken into account. It is encouraging that fluxes measured in the energy ranges 300-1000 MeV and > 1000 MeV, and derived spectral indices show no evidence for variability. For this reason, analyses in this thesis are primarily performed at energies greater than 100 MeV.

5.2 Pulse Profile

Temporal analysis of the Crab pulsar is affected by the significant amount of radio timing noise and frequent glitches which have long been observed from this pulsar. Radio timing is further complicated by the presence of the Crab supernova remnant, which adds to the interstellar scintillation effects. For these reasons, the Crab is one of the most regularly monitored pulsars in the sky. Through a coordinated effort with radio astronomers, contemporaneous timing solutions are available for all of the observations in Table 5.1, such that equation (4.13) can be used to determine the pulsar phase to within 1% of the rotation cycle for all of the *EGRET* γ-rays. The ephemerides used in the temporal analysis of the Crab pulsar are listed in Table 5.2. Each set of timing parameters is known to be valid over the range of dates listed in the first column. The quantities T_0, f_0, f_1, and f_2 refer to the epoch, pulsar frequency, and frequency derivatives, respectively, in equation (4.13). The epoch is given in units of Modified Julian Days (MJD). The value of $\Delta T_{\oplus}$ listed in the last column is the amount of time after 0^{h} UTC on the epoch day that a main radio pulse would arrive at the center of the Earth if there were no dispersion delays. The radio pulse for the Crab pulsar is defined as the "center of mass" of the first peak in the radio pulse profile, which turns out to coincide with the highest point of the peak. The first peak is distinguished by having a leading precursor component at frequencies below 600 MHz. Although there is some overlap between the timing solutions listed in Table 5.2, no observation in Table 5.1 is fully covered by more than one timing solution. The γ-ray arrival times were converted to SSB time using the radio pulsar J2000 position of $\alpha = 05^{\mathrm{h}}34^{\mathrm{m}}31\overset{\mathrm{s}}{.}973$, $\delta = +22°00'52\overset{''}{.}06$ to calculate $\hat{\mathbf{n}}$ in equation (4.22) and equation (4.23).

The Crab γ-ray phase histogram above 100 MeV is presented in Figure 5.5, consisting of the 6015 γ-ray events arriving within an angle θ_{67} of the Crab radio pulsar position, where θ_{67} is defined in equation (3.1). The radio pulse profile at 370 MHz is shown in the top panel for comparison. As expected, the γ-ray lightcurve is aligned with the radio pulse profile. In both cases, the main peak precedes a broader second peak by ~ 0.4 in phase.

To examine the energy-dependent behavior of the Crab γ-ray pulse profile, phase histograms are plotted for four independent energy ranges in Figure 5.6. The phase interval has been divided into the eight components defined in Table 5.3 and indicated by dashed lines in Figure 5.6. These boundary intervals differ from those of Clear et al. (1987) and Nolan et al. (1993) because the increase in data has allowed analysis to be performed on

Table 5.2: Radio Timing Parameters of the Crab Pulsar

Valid Dates	T_0 (MJD)	f_0 (s^{-1})	f_1 (10^{-10} s^{-2})	f_2 (10^{-20} s^{-3})	$\Delta T_\oplus$ (ms)
1991 Mar 16–Jun 5	48371	29.9492515379593	-3.77657	0.818	8.3
1991 May 30–Aug 25	48449	29.9467067038240	-3.77575	1.06	23.8
1992 Jun 28–Oct 18	48857	29.9334039601096	-3.77156	1.16	1.5
1992 Dec 27–1993 Apr 11	49035	29.9276050289288	-3.76972	1.05	25.8
1993 Apr 6–Jul 5	49128	29.9245763662884	-3.76877	1.01	15.5
1993 Nov 5–1994 Jan 27	49337	29.9177729429376	-3.76650	1.32	23.0
1993 Dec 19–1994 Feb 28	49375	29.9165363960966	-3.76612	0.921	4.9
1994 Jun 23–Nov 15	49598	29.9092823758179	-3.76380	1.30	26.3

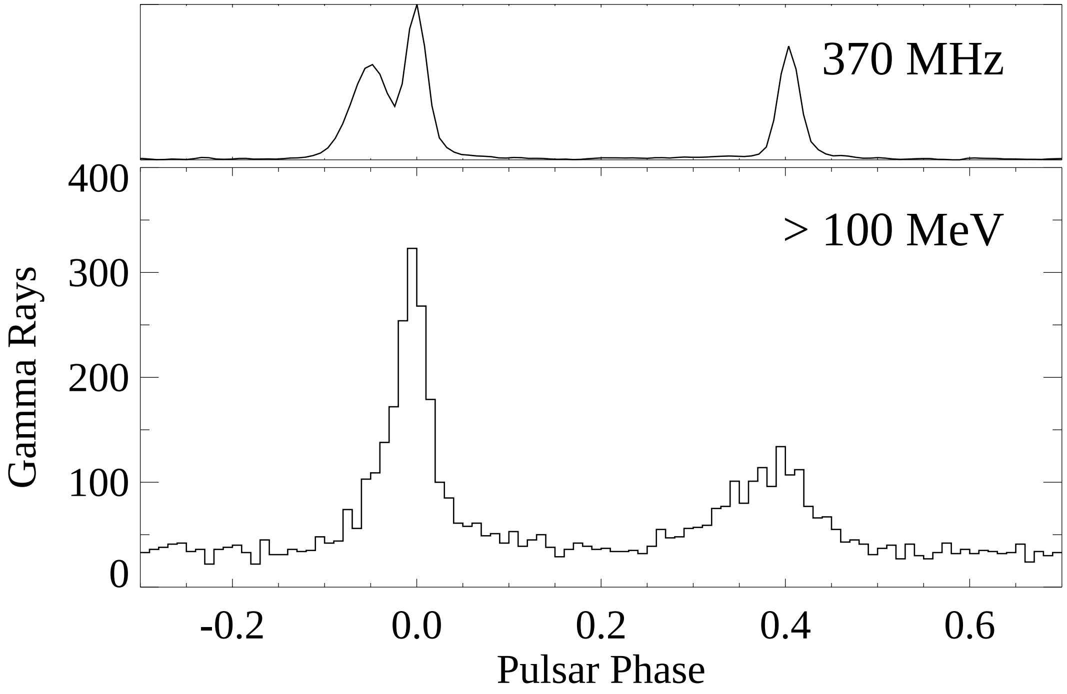

Figure 5.5: Crab radio and γ-ray pulse profiles. The upper panel shows the radio profile at 370 MHz, while the lower panel plots the γ-ray phase histogram formed by epoch-folding all events above 100 MeV accumulated during the observations listed in Table 5.1. The histogram consists of 100 phase bins. The pulsar phase is defined so that the main radio peak occurs at zero.

a finer scale. Note that as the energy increases, the level of background counts drops off significantly. This reflects both the soft spectral nature of the diffuse background emission and the fact that the *EGRET* point spread function becomes much narrower at higher energies, allowing a significant amount of diffuse emission to be eliminated without losing

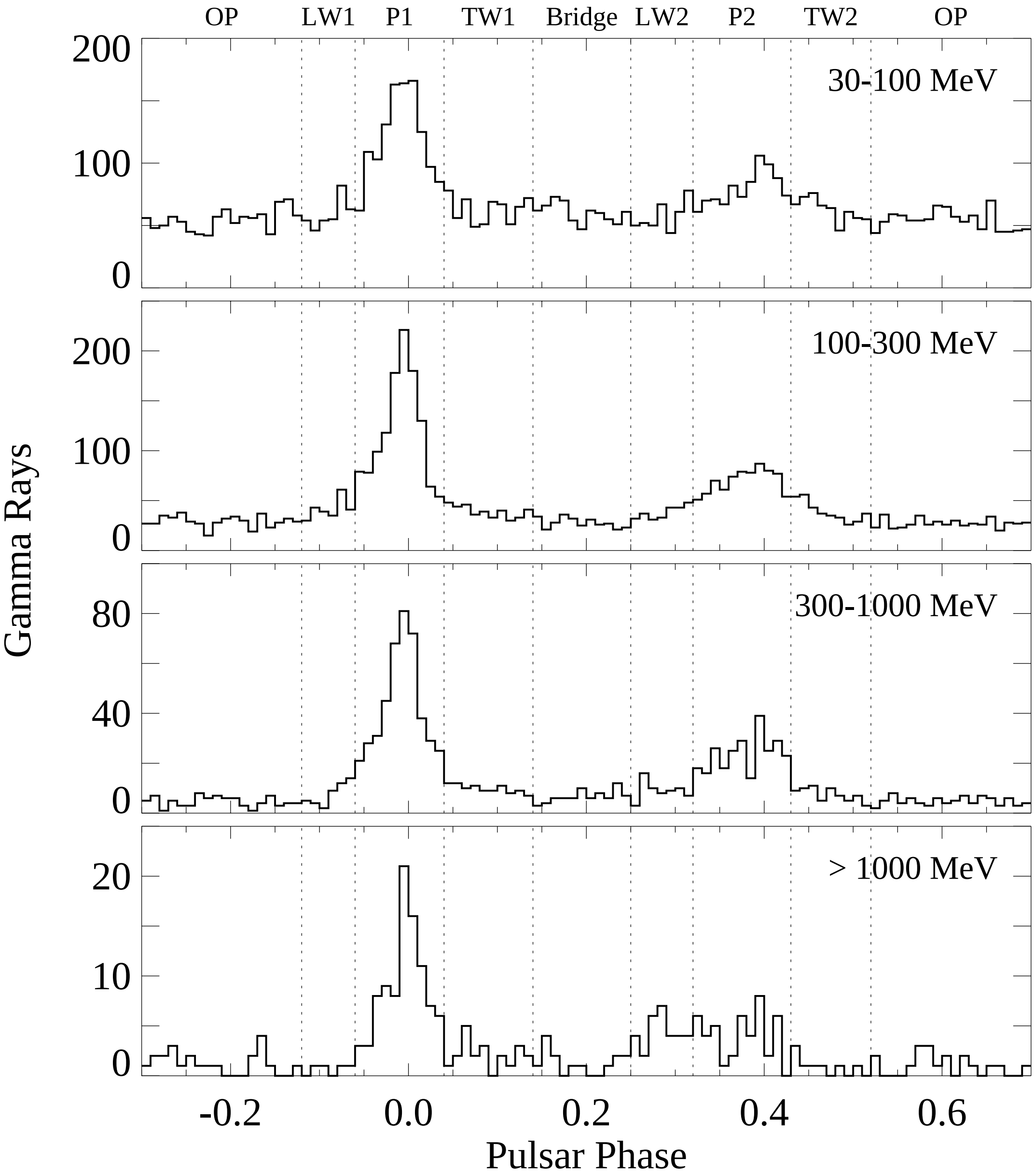

Figure 5.6: Crab γ-ray phase histograms over four independent energy intervals. The vertical dashed lines indicate the definitions of the pulse profile components listed in Table 5.3. Each histogram consists of 100 phase bins.

Table 5.3: Crab Pulsar Phase Interval Definitions

Component	Name	Phase Interval
Leading Wing 1	LW1	0.88 – 0.94
Peak 1	P1	0.94 – 0.04
Trailing Wing 1	TW1	0.04 – 0.14
Bridge	Bridge	0.14 – 0.25
Leading Wing 2	LW2	0.25 – 0.32
Peak 2	P2	0.32 – 0.43
Trailing Wing 2	TW2	0.43 – 0.52
Offpulse	OP	0.52 – 0.88

a large amount of signal. While the ratio of the first peak (P1) to the second peak (P2) appears relatively steady with energy, the leading wing of the second peak (LW2) becomes much more significant as the energy increases, to the extent that it is roughly as prominent as P2 above 1 GeV.

Using the phase definitions of Table 5.3, the "center of mass" of the first γ-ray peak is found to be at phase 0.99 ± 0.03 relative to the main radio peak, showing there is no measurable phase offset between the radio and γ-ray profiles. Varying the phase boundary definition of P1 or the assumed background level has little effect on this result. The center of mass of the second γ-ray peak occurs at phase 0.38 ± 0.04. The separation between the two γ-ray peaks is 12.9 ± 1.6 ms, consistent with the radio separation of 13.5 ms.

5.3 Long-Term Temporal Variation

It has been reported previously (Wills et al. 1982; Özel & Mayer-Hasselwander 1984; Clear et al. 1987; Nolan et al. 1993) that the relative strengths of the two Crab γ-ray peaks may be undergoing a long-term variation. The lightcurves for 10 separate observations of the Crab region performed over more than three years are presented in Figure 5.7. Although the basic shape of the lightcurve appears steady, a more quantitative test is in order. One method is to perform the standard likelihood analysis only on those γ-rays which fall within the phase intervals of the two peaks. The advantage of this method is that it is relatively insensitive to the background emission level. This is important since it is possible that the γ-ray sources in the galactic anticenter region may be time variable. The temporal variation of flux in the phase intervals P1 and P2, as well as the variation in their ratio P2/P1, is shown in Figure 5.8. Assuming a Gaussian distribution about constant flux levels, the data points have χ^2 values of 17.9, 7.5, and 6.2 for P1, P2, and P2/P1, respectively, which for nine degrees of freedom indicates that there is no substantial variation in either the peak

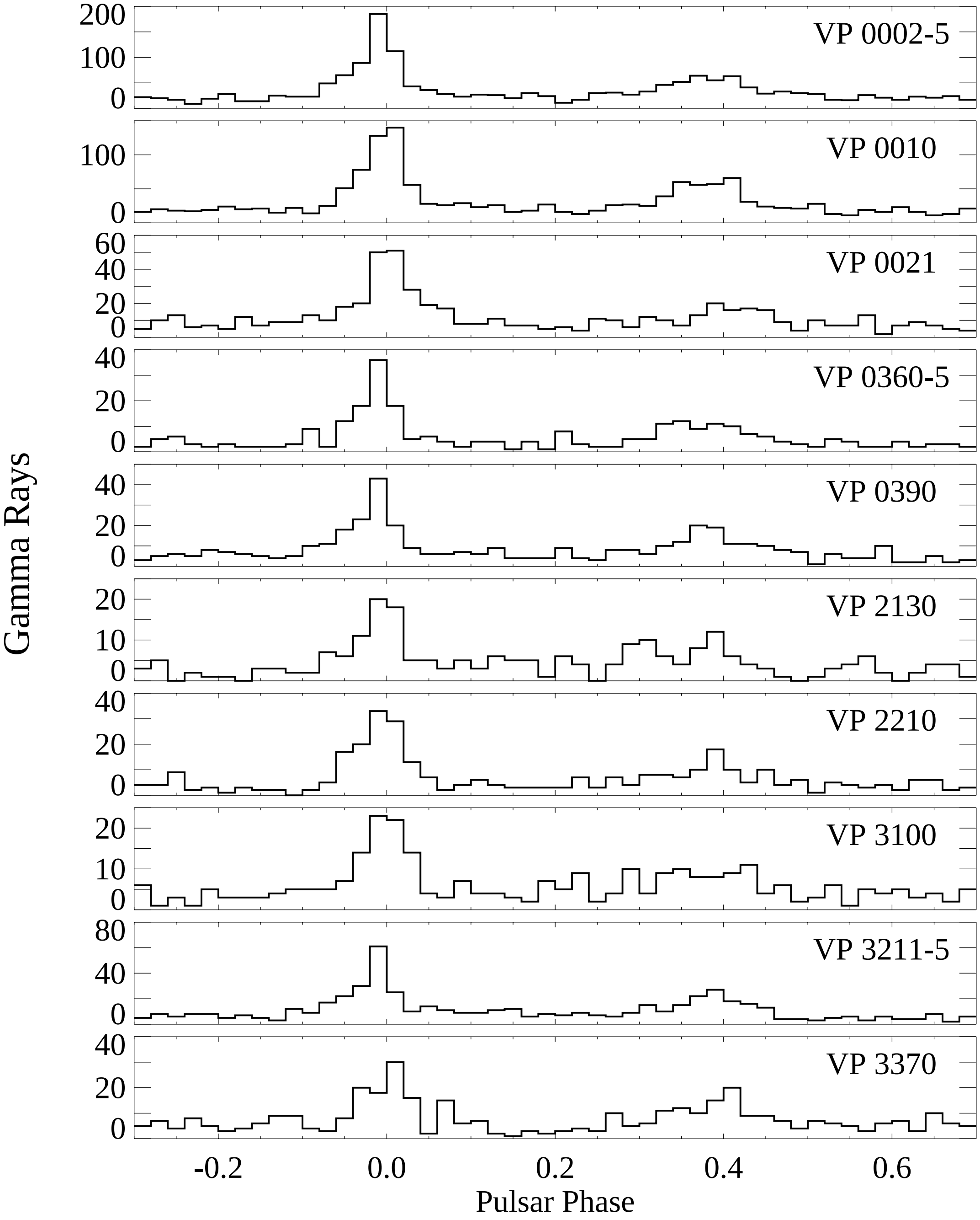

Figure 5.7: Crab pulse profiles above 100 MeV for the *EGRET* observations listed in Table 5.1. Consecutive observations have been combined. Each lightcurve consists of 50 bins.

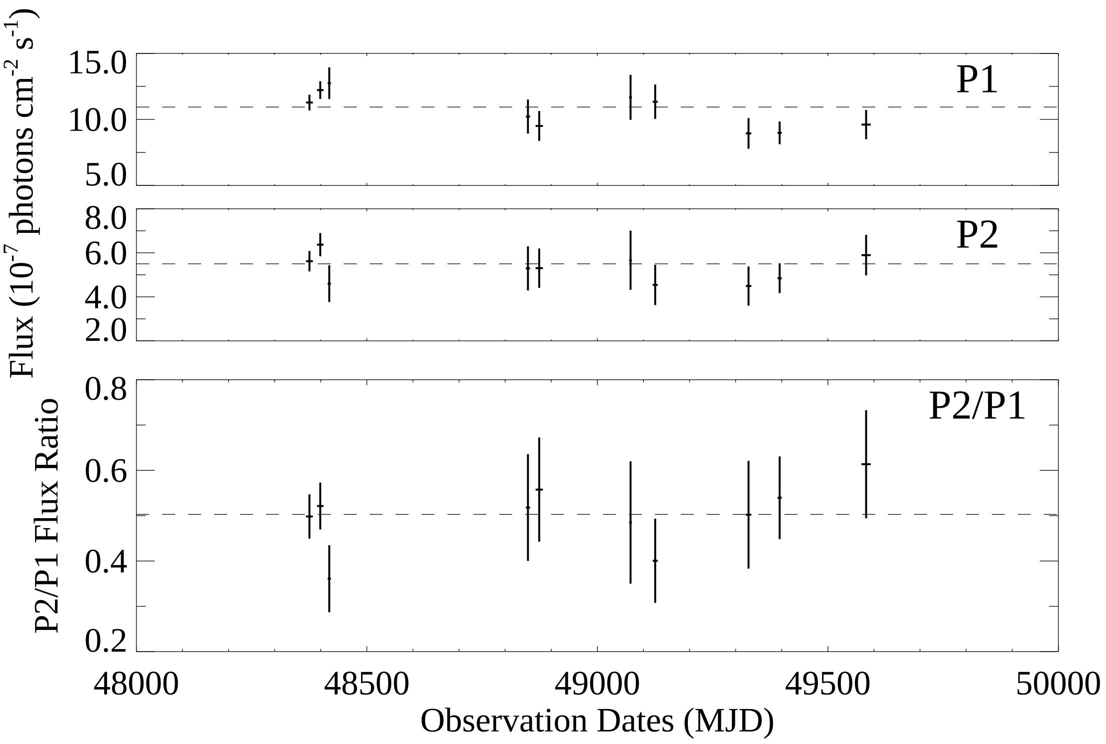

Figure 5.8: Temporal variation of the Crab pulsar total γ-ray flux above 100 MeV from the first peak (upper panel), second peak (center panel), and ratio of the flux from the second peak to that of the first peak (lower panel). The dashed line in each plot indicates the value determined from all of the data combined.

Table 5.4: *COS B* Definition of Phase Intervals of Crab Pulsar

Region	Phase Interval
First Pulse	0.94 – 0.04
Inter-region	0.04 – 0.32
Second Pulse	0.32 – 0.46
Background	0.46 – 0.94

fluxes or their ratio.

The above analysis does not take into account a possible unpulsed component from the Crab nebula, which could obscure the variability in the peak ratio. Assuming that the emission in the offpulse phase region represents the combined unpulsed flux from the background and nebula, the number of background counts may be estimated from the offpulse phase interval, and the total number of counts detected in P1 and P2 phase can be adjusted accordingly. To be consistent with analyses performed on the *SAS 2* and *COS B* datasets, the analysis here is performed over the energy range 50–3000 MeV using the

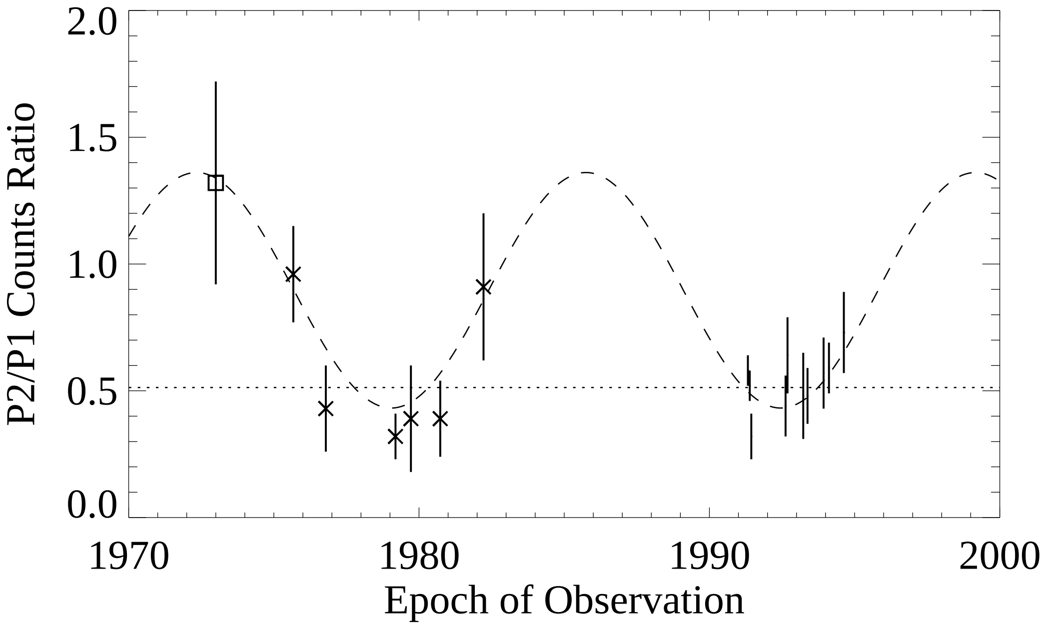

Figure 5.9: Temporal variation of the counts ratio of the second Crab pulsar peak to the first for the energy range 50–3000 MeV. The *SAS 2* data point (Kanbach 1990) determined for $E > 35$ MeV is marked by a square. The *COS B* data points (Clear et al. 1987) are denoted by crosses. The dashed line indicates the best fit of a sinusoidal function to all data points, while the weighted average of ratios are represented by the dotted line.

phase boundaries in Table 5.4, which match those used by Wills et al. (1982). The P2/P1 counts ratio derived from *SAS 2*, *COS B*, and *EGRET* data are plotted in Figure 5.9. The weighted average of the ratios is 0.51 ± 0.03, with a χ^2 value of 27 for 16 degrees of freedom, which implies that the probability that these variations are due to statistical fluctuations is 4.1%. Kanbach (1990) suggested that the relative strengths of the two peaks might be undergoing a sinusoidal variation of the form

$$\mathrm{P2/P1} = a + b \sin 2\pi \left(\frac{t - t_0}{T} \right) , \tag{5.2}$$

perhaps due to the free nutation of the neutron star. A least squares fit of this function to the *SAS 2*, *COS B*, and *EGRET* data converged for a dc level $a = 0.90 \pm 0.13$, amplitude $b = 0.46 \pm 0.15$, offset $t_0 = 1982.4 \pm 0.4$ yr, and period $T = 13.4 \pm 0.6$ yr. This fit is shown in Figure 5.9 to agree very well with the data, generating a χ^2 deviation of 13.0 with 13 degrees of freedom. It is also consistent with the fit determined by Kanbach (1990) solely from the *SAS 2* and *COS B* data. It should be kept in mind, however, that comparing results from different detectors is somewhat complicated. The *SAS 2* detector had limited energy resolution, and so the data point for 1972 plotted in Figure 5.9 is actually determined for $E > 35$ MeV. In addition, the effective sensitive area of each instrument will undoubtedly have different spectral behavior. If the two peaks have different spectral indices, the P2/P1 ratio will be different for each instrument. Similarly, if the spectral response of an instrument changes over its lifetime, as is the case for *EGRET*, the P2/P1 ratio may be affected. If the *EGRET* points are considered by themselves, the P2/P1 counts ratio is consistent with an average ratio 0.52 ± 0.03, measuring a χ^2 deviation of 9.5 for nine degrees of freedom. The only evidence of variability comes from including the results of previous detectors. Still, the current *EGRET* data points were measured during a time when the modeled sinusoidal curve was at an inflection point, so a more definitive test of the possible periodic variation of the ratio of the strength of the two peaks will come towards the end of the *CGRO* mission.

A more general question is whether the γ-ray pulse profiles determined by *EGRET* show any evidence of variability. To address this question, both a χ^2 test and Kolmogorov-Smirnov (K-S) test were performed for the observations listed in Table 5.1. The standard χ^2 statistic for comparing two binned distributions R and S is

$$\chi^2 = \sum_{i=1}^{N} \frac{(S_i - nR_i)^2}{\sigma_{S_i}^2 + n^2\sigma_{R_i}^2} \, , \tag{5.3}$$

where the sum is taken over all N bins, and $n = S/R$ is a normalization factor which adjusts for the fact that $S = \sum S_i$ is not necessarily equal to $R = \sum R_i$. Due to the variability of neighboring sources, it is expected that the background count level will vary from observation to observation. Since the only concern here is whether the actual pulse shape is consistent, care must be taken to exclude the possible effect of a variable background level. This is achieved by subtracting off a normalized component determined from the offpulse region as follows

$$S_i' = S_i - fB_S \, . \tag{5.4}$$

Here, S_i' is the adjusted number of counts in a bin, B_S is the number of counts from the S distribution falling in the offpulse region of phase width $\Delta\phi$, and $f = (N\Delta\phi)^{-1}$ is the scaling factor used to determine the number of background counts per bin. The variance of S_i' is then determined from Poisson statistics to be

$$\sigma_{S_i'}^2 = S_i + f^2 B_S \, . \tag{5.5}$$

Table 5.5: Crab Measured Characteristics for the *EGRET* Observations

Viewing Period	Total Flux 10^{-6} cm^{-2} s^{-1} ($>$ 100 MeV)	Spectral Index (100–10000 MeV)	P2/P1 Counts Ratio (50–3000 MeV)	χ^2 Prob (25 bins)	K-S Prob
0002–5	2.5 ± 0.1	-2.15 ± 0.05	0.58 ± 0.06	17.7%	18.7%
0010	2.6 ± 0.1	-2.18 ± 0.06	0.52 ± 0.06	31.3	3.8
0021	2.8 ± 0.2	-2.29 ± 0.10	0.32 ± 0.09	1.2	3.7
0360–5	2.0 ± 0.2	-2.03 ± 0.14	0.44 ± 0.12	42.8	28.2
0390	2.2 ± 0.2	-2.31 ± 0.13	0.64 ± 0.15	23.0	8.5
2130	2.3 ± 0.3	-2.01 ± 0.15	0.48 ± 0.17	4.7	32.7
2210	2.0 ± 0.2	-2.00 ± 0.12	0.48 ± 0.11	3.2	57.2
3100	1.9 ± 0.2	-2.10 ± 0.15	0.57 ± 0.14	45.1	27.1
3211–5	2.0 ± 0.2	-1.93 ± 0.09	0.59 ± 0.10	1.7	12.2
3370	2.4 ± 0.2	-2.02 ± 0.10	0.73 ± 0.16	0.4	1.0

The modified χ^2 statistic thus becomes

$$\chi^2 = \sum_{i=1}^{N} \frac{[S_i - n'R_i - f(B_S - n'B_R)]^2}{S_i + n'^2 R_i + f^2(B_S + n'^2 B_R)} \, , \tag{5.6}$$

where B_R is the number of offpulse counts in the R data set, and $n' = (\sum S_i')/(\sum R_i')$ is the adjusted scaling factor between the two data sets. Since both the background and source counts are scaled, the number of degrees of freedom is $N - 2$. In effect, this method will determine the consistency of the pulse profile relative to the average level of the offpulse region.

The K-S test measures the maximum difference between two cumulative unbinned distributions (e.g. Press et al. 1992). Unfortunately, there is no simple way to account for the different levels of background, but the background component is evenly distributed along the pulse profile and should not vary radically, so significant errors will not be introduced. The phase distribution from each observation was compared to the distribution obtained from the sum of the other observations, ensuring that the two data sets are independent. A number of characteristics determined for each *EGRET* observation of the Crab complex are presented in Table 5.5. The viewing period, total measured flux, derived spectral index, and P2/P1 counts ratio are listed in the first four columns. The results of the χ^2 test for 25 bins and the K-S test on the are presented in the fifth and sixth columns, respectively. These quantities are expressed in terms of the probability that the set of phases in an observation is drawn from the same distribution as the sum of the phases in the other observations. While the χ^2 and K-S probabilities are slightly on the small side, the overall evidence for variability is not significant. VP 3370 is the only observation which measures low probabilities with both the χ^2 and K-S tests. Particularly interesting is the fact that the previous observations VP 3211–5 also have moderately small values for both the χ^2 and K-S tests. However, when the two sets of observations are combined and tested against the other data sets, the χ^2 probability of correlation is 73.8% for 50 bins, and the K-S test probability is 65.5%. Hence, the pulse profiles formed from the latter observations are consistent with those formed from the earlier observations.

The low χ^2 probabilities in Table 5.5 appear to result from the low number of counts in the bridge and offpulse region, where the assumed variance $\sigma_i^2 = N_i$ for N_i counts in a bin is an inadequate approximation. For the observation VP 3370, the bin from phase 0.12–0.16 contributes 16.4 to the total χ^2 value of 44.9, implying that there is a $\sim 4\sigma$ deviation in that bin. Examination of the data shows that this bin contains $N_i = 3$ counts, compared to the 11.5 ± 1.2 counts expected from the background-adjusted phase histogram formed from the other observations. From the Poisson counting statistics, the actual probability of measuring 3 counts when 11.5 are expected given by equation (4.4) to be 0.3%, not nearly the 4σ deviation derived using the large count approximation.

In the absence of significant evidence of long-term variability from any component of the Crab pulse profile, it will be assumed throughout the rest of this chapter that the Crab pulsar and nebula characteristics are consistent over the nearly three and a half years of *EGRET* observations, and the data from separate observations can be combined without loss of generality.

5.4 Phase-Resolved Analysis

The energy-dependent nature of the Crab pulse profile morphology can be seen from Figure 5.6. To quantify this behavior, standard analysis techniques are performed on individual components of the Crab pulse profile. This is a straightforward matter of analyzing only those γ-rays which fall within a designated phase interval. Since the statistics for the Crab pulsar are high, it is possible to divide the pulse profile into many smaller subintervals and perform likelihood analysis on these data subsets. The advantage of a phase-resolved spatial analysis over a simple lightcurve analysis is that excesses above the predicted background are required to be distributed according to the instrument point spread function before being attributed to the pulsar.

The pulse profile is divided into twenty equal width phase bins ($\Delta\phi = 0.05$), and spatial counts maps are formed from the γ-rays in each phase bin. The results of the likelihood analysis above 100 MeV are shown in Figure 5.10. The center plot shows $\mathrm{TS}^{1/2}$ measured

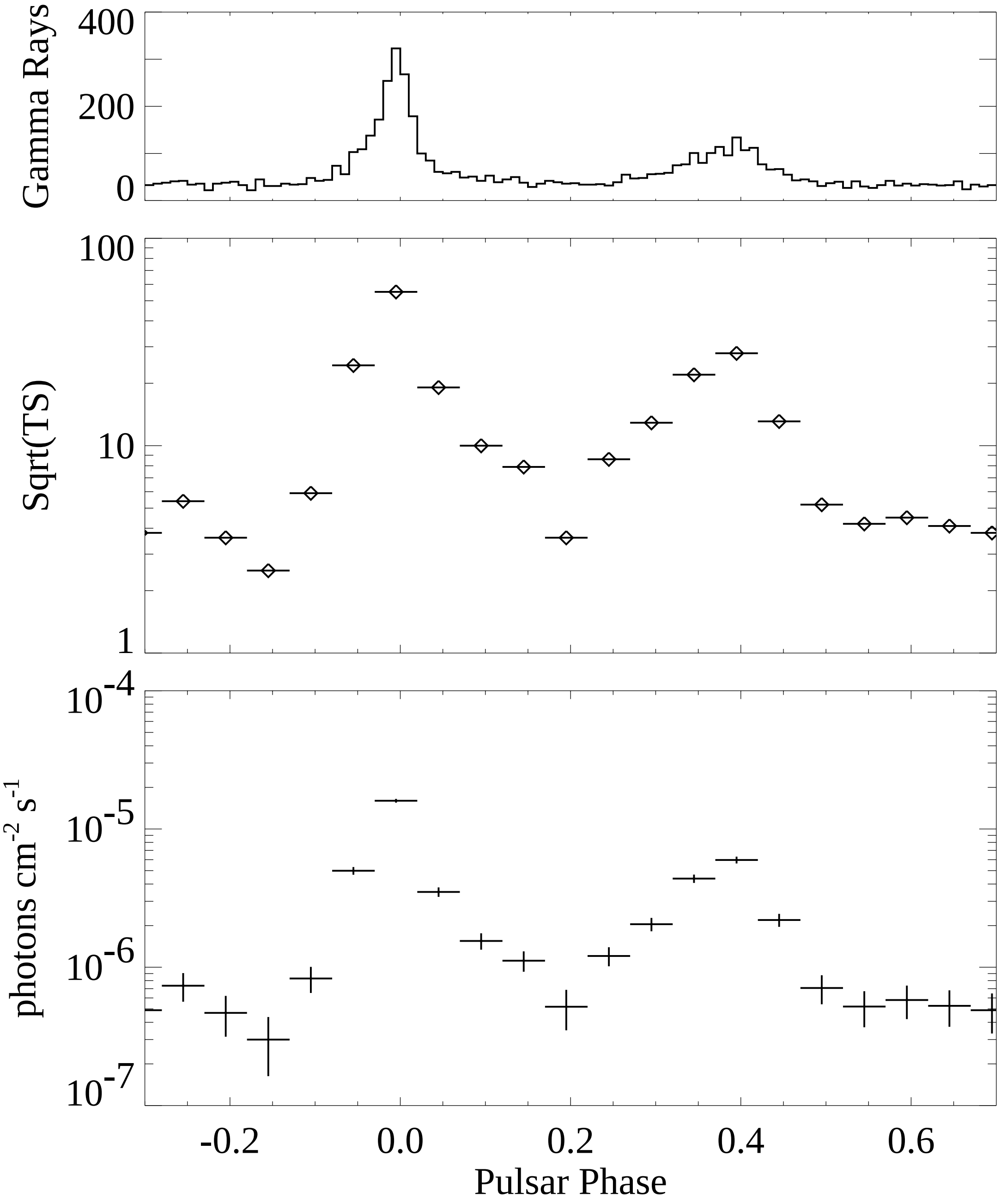

Figure 5.10: Phase-resolved likelihood analysis of the Crab pulse profile above 100 MeV. For reference, the top panel shows the lightcurve formed from epoch-folding all events within θ_{67} of the Crab pulsar. The center panel shows $\mathrm{TS}^{1/2}$ derived from likelihood analysis for each phase bin, and the lower panel shows the corresponding instantaneous flux above the diffuse background level.

from likelihood analysis for each of the twenty phase bins. Since the Crab pulsar position is fixed in this analysis, $\mathrm{TS}^{1/2}$ is approximately the detection significance of each phase bin. Emission is from the Crab complex over the entire pulse profile, with the weakest phase bin measuring $\mathrm{TS}^{1/2} = 2.5$, and 16 of the 20 bins detected with $\mathrm{TS}^{1/2} > 4$. The lower panel in Figure 5.10 shows the level of instantaneous flux above the background emission level. The total level of emission from Crab is the average of the plotted values. The values are plotted on a logarithmic scale since the flux varies by almost two orders of magnitude across the pulse profile, with the single bin centered about the first peak accounting for ~35% of the total Crab emission.

One of the more surprising features of Figure 5.10 is the precipitous drop in flux for the phase bin at $\phi \approx 0.2$. Not only does this bin have a flux level which is ~1/3 that of the preceding phase bin, but its level of emission is consistent with the weakest part of the offpulse region. Previously, there were insufficient statistics to resolve such a feature, and the bridge emission was assumed to be well above the level of offpulse emission at all points. While the level of emission in the offpulse region does not show such dramatic variation, there is some indication that it may also vary with phase, particularly near the LW1 component ($\phi \approx 0.85$). An unpulsed component present in the Crab pulse profile can be no greater than flux measured in the weakest phase bin. Thus, an unpulsed component has a maximum flux of $(3.0 \pm 1.4) \times 10^{-7}$ photons $\mathrm{cm}^{-2}\ \mathrm{s}^{-1}$ flux, or $13 \pm 6\%$ of the total Crab emission above 100 MeV.

There are not enough counts to perform a full spectral analysis for each of the 20 phase bins. Instead, a *hardness ratio* R is defined as

$$R \equiv \frac{F(>300\ \mathrm{MeV})}{F(100--300\ \mathrm{MeV})}\ , \tag{5.7}$$

where $F(100 - 300\ \mathrm{MeV})$ is the likelihood flux measured between 100 and 300 MeV, and $F(>300\ \mathrm{MeV})$ is the likelihood flux measured above 300 MeV, both in units of photons $\mathrm{cm}^{-2}\ \mathrm{s}^{-1}$. A source with a differential flux behaving as a perfect power law above 100 MeV with a spectral index of -2.0 will have a hardness ratio of $R \simeq 0.5$. The hardness ratios calculated for the same phase bins plotted in Figure 5.10 are shown in Figure 5.11. There is no data point plotted for the bin centered at phase $\phi \approx 0.85$ because the paucity of counts in that bin prevented a detection in the 100–300 MeV energy range. The most striking aspect of this plot is the absence of a strong correlation to the features in the pulse profile. The hardness ratio increases smoothly as the pulsar phase moves across the first pulse, leveling out in the bridge region before reaching its maximum value in the leading wing of the second peak ($\phi \approx 0.25$). The emission from this bin is only detected with

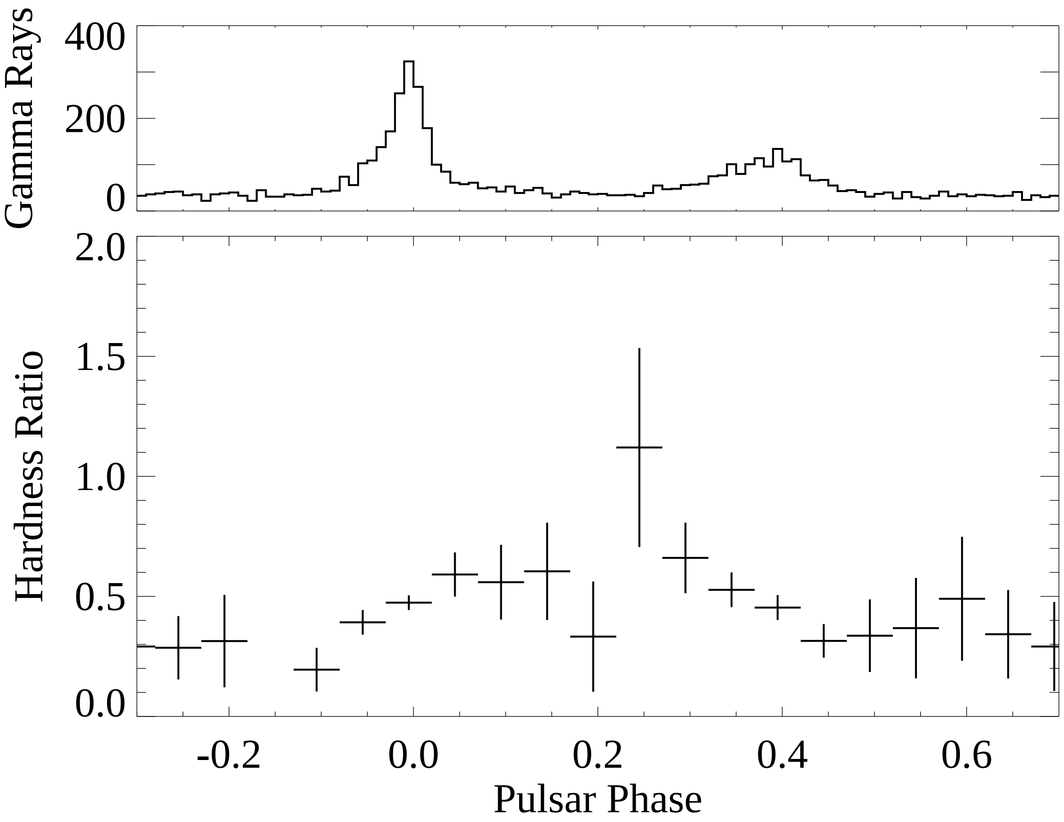

Figure 5.11: Hardness ratio throughout the Crab pulse profile. The top panel shows the γ-ray lightcurve above 100 MeV for reference.

$TS^{1/2} = 3.6$ from 100–300 MeV, but is detected at a significance of $TS^{1/2} = 9.1$ above 300 MeV. The weak detection in the lower energy range leads to the very large error bar. As the phase increases through the second peak, the hardness ratio decreases back to the soft level of the offpulse emission. It is interesting that the extreme hardness ratios are in the bridge and offpulse phase intervals, not near the two peaks which dominate the pulsar lightcurve.

The phase-resolved spectral behavior over the entire *EGRET* energy range is presented in Figure 5.12, which show the photon spectra derived from likelihood spatial analysis of the phase intervals defined in Table 5.3. For each component, a spectral fit is only performed over the energy interval for which the data points were reasonably consistent with a power law distribution. The energy ranges, spectral indices, photon flux predicted at 100 MeV by the power law fit, χ^2 per degree of freedom (DOF), and DOF for each fit are listed in Table 5.6. The fits discussed here are with respect to the instantaneous differential photon flux for each component. The time-averaged solutions are obtained by multiplying the flux

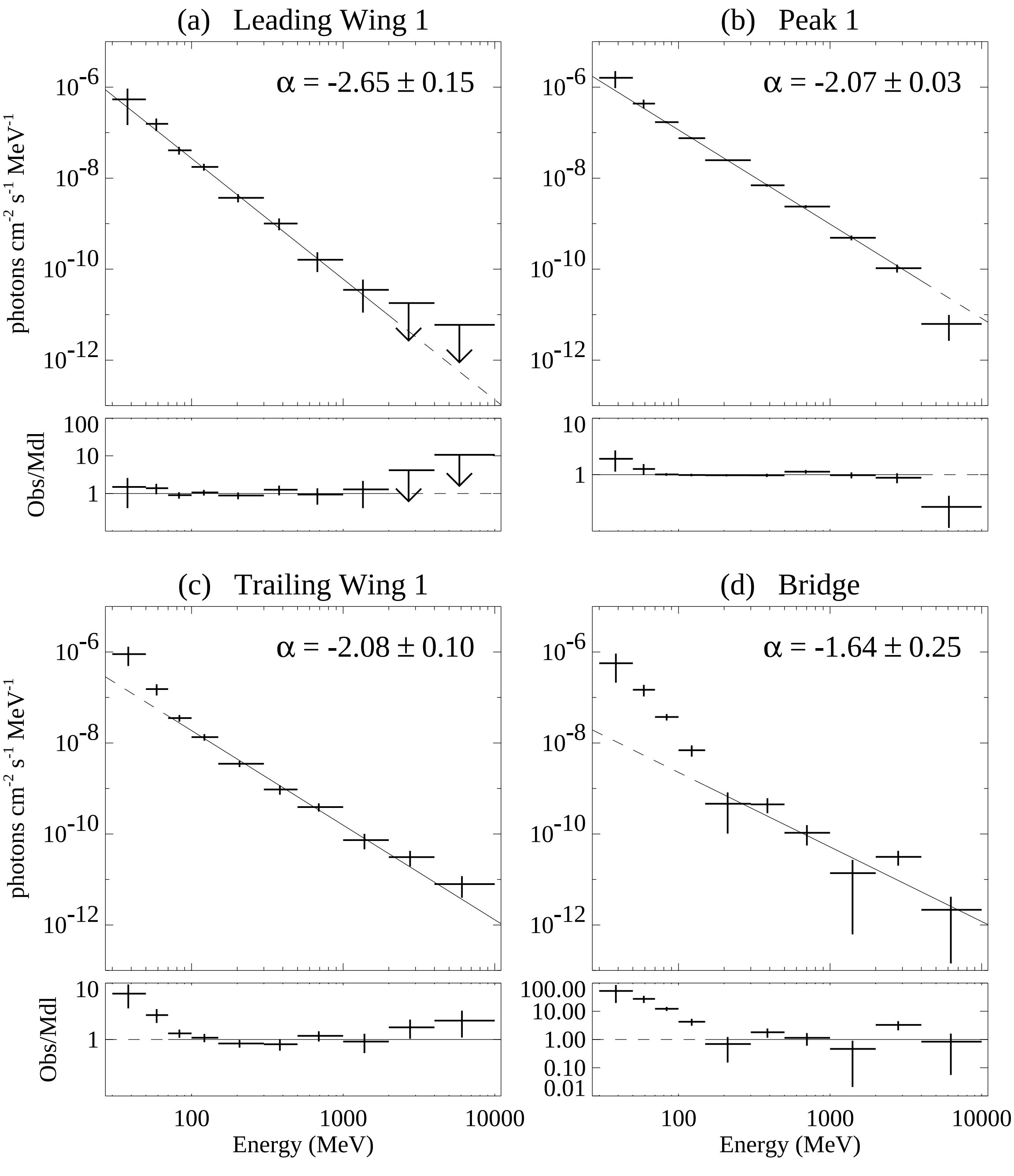

Figure 5.12: Differential photon spectra derived from likelihood spatial analysis of the Crab first pulse (a) leading wing, (b) peak, and (c) trailing wing, as well as the (d) bridge phase intervals. The power law fit is indicated by a solid line with the spectral index α listed for each component. The upper limits in (a) are 2σ.

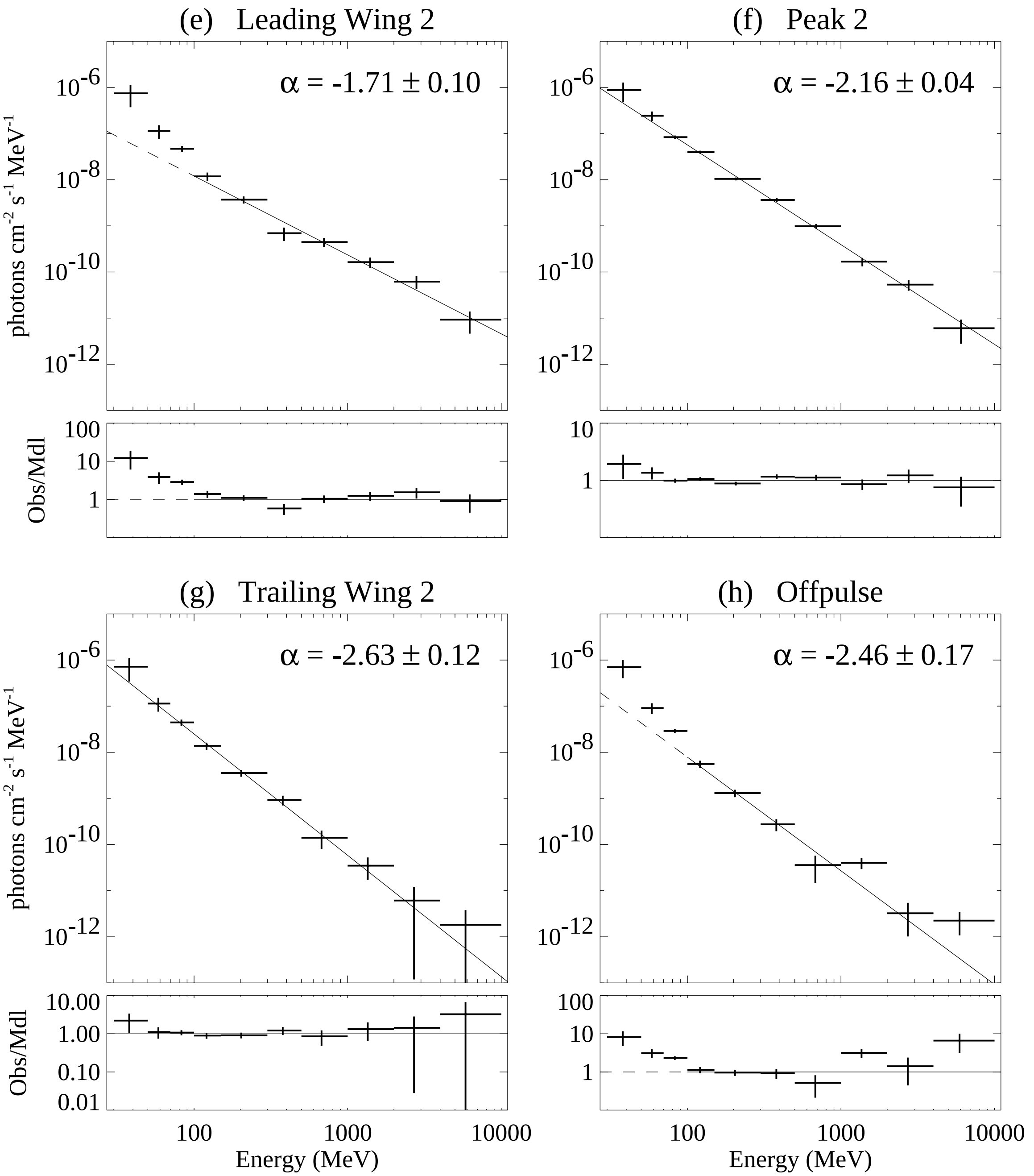

Figure 5.12: (continued) Differential photon spectra derived from likelihood spatial analysis of the Crab second pulse (e) leading wing, (f) peak, and (g) trailing wing, and the (h) offpulse phase intervals.

Table 5.6: Crab Pulsar Component Spectral Fits

Component	Energy Range (MeV)	Spectral Index	$F_{100}{}^a$	χ^2/DOF	DOF
LW1	30 – 2000	-2.65 ± 0.15	2.7 ± 0.3	0.41	6
P1	30 – 4000	-2.07 ± 0.03	11.5 ± 0.4	0.82	7
TW1	50 – 10000	-2.08 ± 0.10	1.9 ± 0.2	1.14	6
Bridge	150 – 10000	-1.64 ± 0.25	0.2 ± 0.1	1.80	4
LW2	100 – 10000	-1.71 ± 0.10	1.2 ± 0.2	1.78	5
P2	30 – 10000	-2.16 ± 0.04	5.7 ± 0.3	1.37	8
TW2	30 – 10000	-2.63 ± 0.12	2.5 ± 0.2	0.44	8
OP	100 – 10000	-2.46 ± 0.17	0.8 ± 0.1	2.50	5

---

[a] Modelled instantaneous differential flux at 100 MeV in units of 10^{-8} photons cm^{-2} s^{-1} MeV^{-1}

Table 5.7: Crab Double Power Law Spectral Fits

	Power Law 1		Power Law 2		χ^2
Component	F_1(100 MeV)*	α_1	F_2(100 MeV)*	α_2	(6 DOF)
Total	0.7 ± 0.2	-4.89 ± 0.66	2.3 ± 0.3	-2.05 ± 0.04	11.04
TW1	0.6 ± 0.4	-5.27 ± 1.00	1.3 ± 0.4	-1.86 ± 0.13	6.06
Bridge	1.2 ± 0.3	-4.33 ± 0.47	0.1 ± 0.1	-1.42 ± 0.36	10.26
LW2	1.6 ± 0.4	-3.97 ± 0.69	0.7 ± 0.4	-1.51 ± 0.16	4.02
OP	1.0 ± 0.2	-4.13 ± 0.46	0.2 ± 0.2	-1.76 ± 0.29	2.40

* Modelled instantaneous differential flux in units of 10^{-8} photons cm^{-2} s^{-1} MeV^{-1}.

values by the phase width of each component.

The spectral fits reflect many of the features suggested by the hardness plot of Figure 5.11. The softest components in the Crab lightcurve are the second pulse trailing wing (TW2), offpulse (OP), and first pulse leading wing (LW1) components. The pulsar emission is hardest in the leading wing of the second pulse (LW2). The only component to show some evidence of a high energy cutoff is P1.

The first pulse trailing wing (TW1), bridge, LW2, and OP components all appear to have a softer spectrum at energies less than 100 MeV which deviates from the power law established above 100 MeV. A similar feature is seen in the total spectrum of Figure 5.2. This implied spectral break is especially apparent for the bridge and offpulse regions, the two weakest components of the Crab pulse profile. To investigate this behavior, the spectra are fit with a double power law of the form

$$\frac{dN}{dE} = I_1\, E^{\alpha_1} + I_2\, E^{\alpha_2} \;\; \text{photons cm}^{-2}\ \text{s}^{-1}\ \text{MeV}^{-1}\ . \tag{5.8}$$

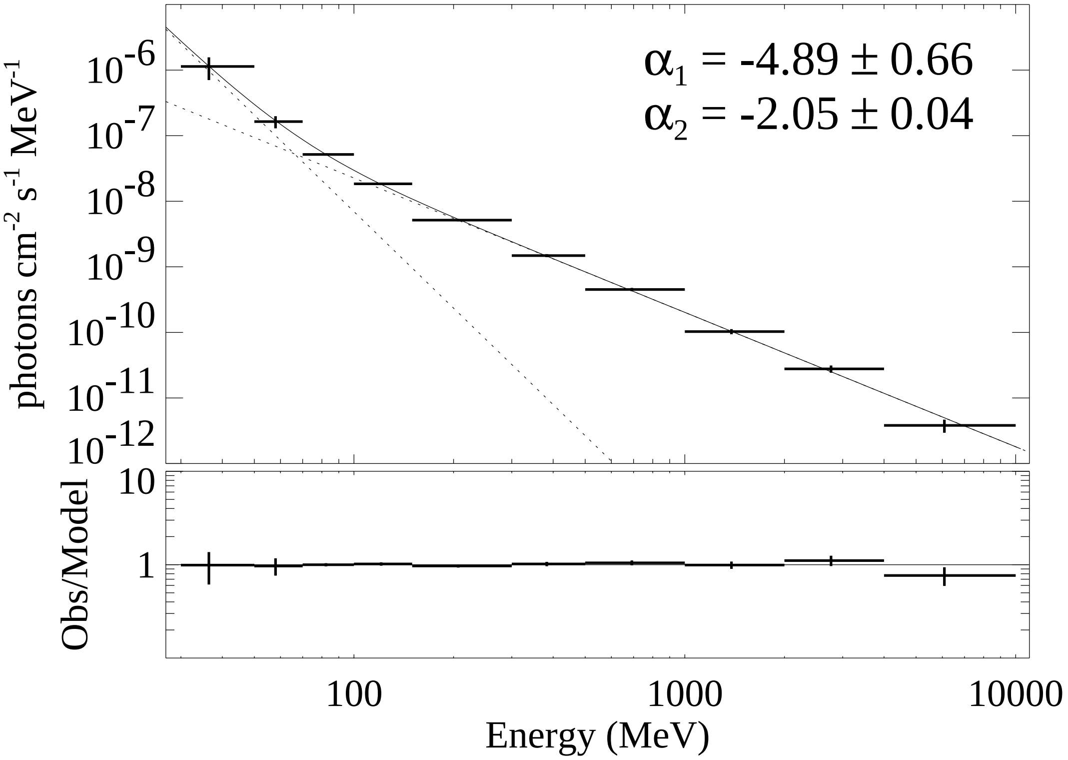

Figure 5.13: Double power law fit to the total Crab emission photon spectrum. The fit has a form given by equation (5.8).

This introduces two additional degrees of freedom when minimizing the $\chi^2(\lambda)$ function of equation (4.49). Figure 5.13 shows the double power law fit to the total Crab emission, and Figure 5.14 shows similar fits to spectra of the TW1, bridge, LW2, and OP components. The various parameters of the double power law fits are listed in Table 5.7. The χ^2 values listed in the sixth column indicate the measured photon spectrum from each component in Table 5.7 is well-modeled by emission from two independent power laws over the energy range 30 MeV–10 GeV. The second and third columns of Table 5.7 show that the soft component is consistently fit with a spectral index of $\alpha_1 \lesssim -4$ and a flux at 100 MeV of $F_1(100 \text{ MeV}) \sim 10^{-8}$ photons cm^{-2} s^{-1}. However, the fourth and fifth columns show that the harder emission varies for each component. It seems clear, then, that there is an unpulsed ultra-soft component to the Crab total emission. Moreover, this ultra-soft emission dominates the pulsar radiation from the bridge and offpulse regions at energies less than ~100 MeV.

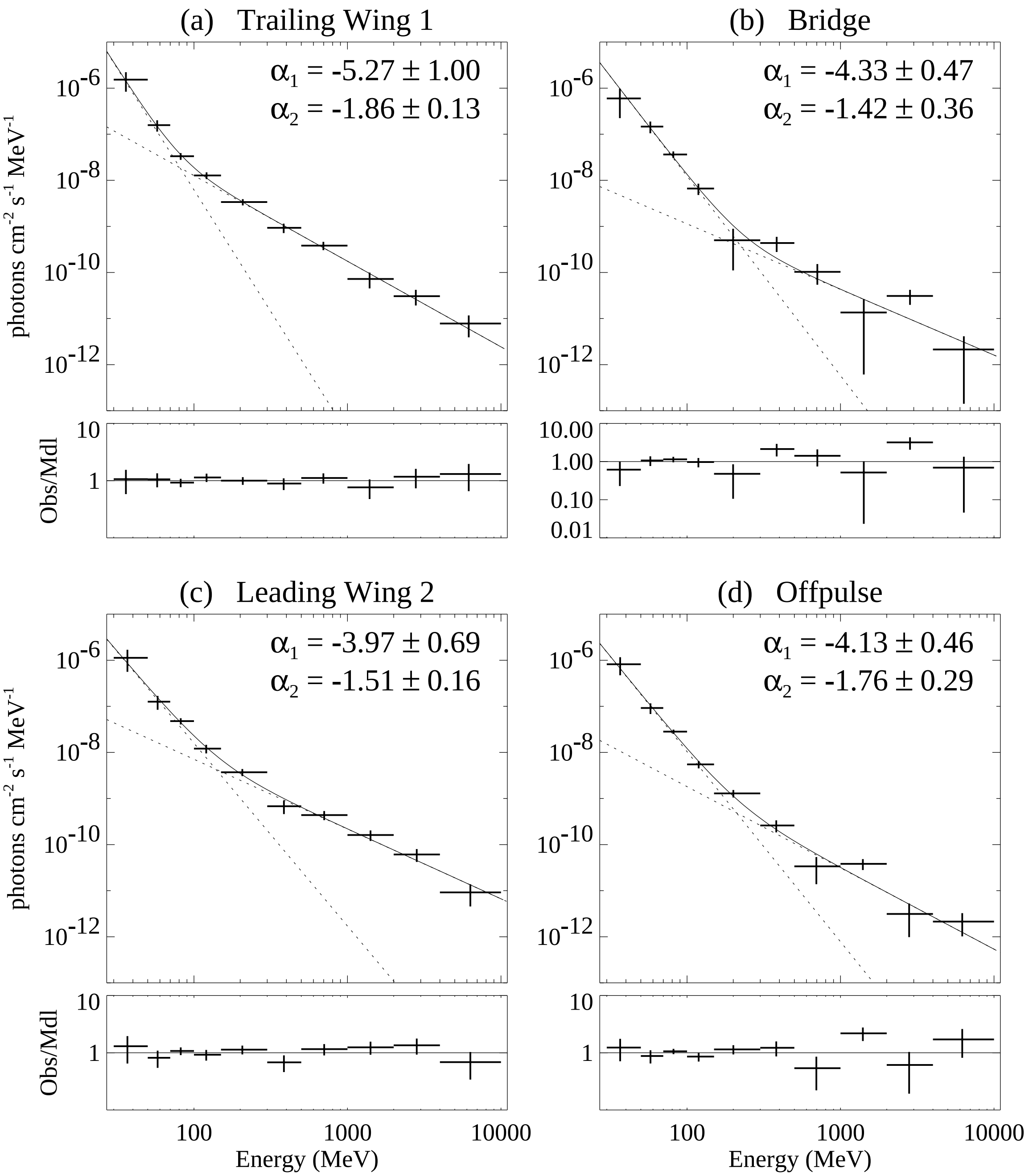

Figure 5.14: Double power law fits to the likelihood-derived photon spectra of the (a) TW1, (b) bridge, (c) LW2, and (d) OP components of the Crab pulse profile.

Table 5.8: Crab Pulsed Analysis Spectral Fits

Component	Energy Range (MeV)	Spectral Index	F_{100}[a]	χ^2/DOF	DOF
Total	50 – 10000	-2.08 ± 0.03	2.61 ± 0.11	3.24	7
LW1	50 – 1000	-2.26 ± 0.18	0.92 ± 0.15	3.95	4
P1	50 – 4000	-2.05 ± 0.03	8.87 ± 0.29	1.77	6
TW1	50 – 10000	-1.88 ± 0.10	0.76 ± 0.11	1.59	7
Bridge	50 – 4000	-1.80 ± 0.31	0.17 ± 0.09	4.72	5
LW2	50 – 30000	-1.69 ± 0.08	0.77 ± 0.11	1.74	8
P2	50 – 30000	-2.13 ± 0.04	4.08 ± 0.19	3.15	8
TW2	50 – 4000	-2.51 ± 0.14	1.09 ± 0.13	2.87	5

---

[a] Modelled instantaneous differential flux at 100 MeV in units of 10^{-8} photons cm^{-2} s^{-1} MeV^{-1}

5.5 Pulsed Spectral Analysis

If the offpulse emission is solely due to the unpulsed nebular emission, then the spectral behavior of the other components can be analyzed in greater detail using a pulsed spectral analysis. In this method, the number of pulsed counts in each phase interval is found by subtracting off a normalized number of unpulsed counts determined from the offpulse region. One advantage of pulsed analysis is that it bases its flux estimates only on the number of counts detected above the normalized background level. Unlike likelihood analysis, pulsed analysis is capable of performing spectral analysis out to 30 GeV. Experience has shown that below 50 MeV, the combination of the reduced *EGRET* sensitive area, large instrumental uncertainties, and dominance of the galactic diffuse radiation prevents the derivation of constraining flux estimates with pulsed analysis. For this reason, pulsed spectral analysis is typically carried out over the energy range 50 MeV–30 GeV.

The pulsed spectra of the components defined in Table 5.3 are plotted in Figure 5.15, with the details of the fits given in Table 5.8. There are no data plotted above 2 GeV for the LW1 component because no counts were detected in this phase interval at the highest energies. Unlike the fits to the spectra derived from likelihood analysis, the pulsed analysis power law fits are of an extremely poor quality. The best fit is to the TW1 component with a χ^2 of 17.2 for 6 degrees of freedom, which still only has a $\sim$ 13% probability level. The poor fits may be a result of subtracting pulsed magnetospheric emission present in the offpulse region from the other components, or it may be an indication that the pulsed Crab emission does not behave as a power law.

It should be noted that the weak components of the pulse profile no longer show a significant steep spectrum emission at lower energies. Subtracting the ultra-soft low energy

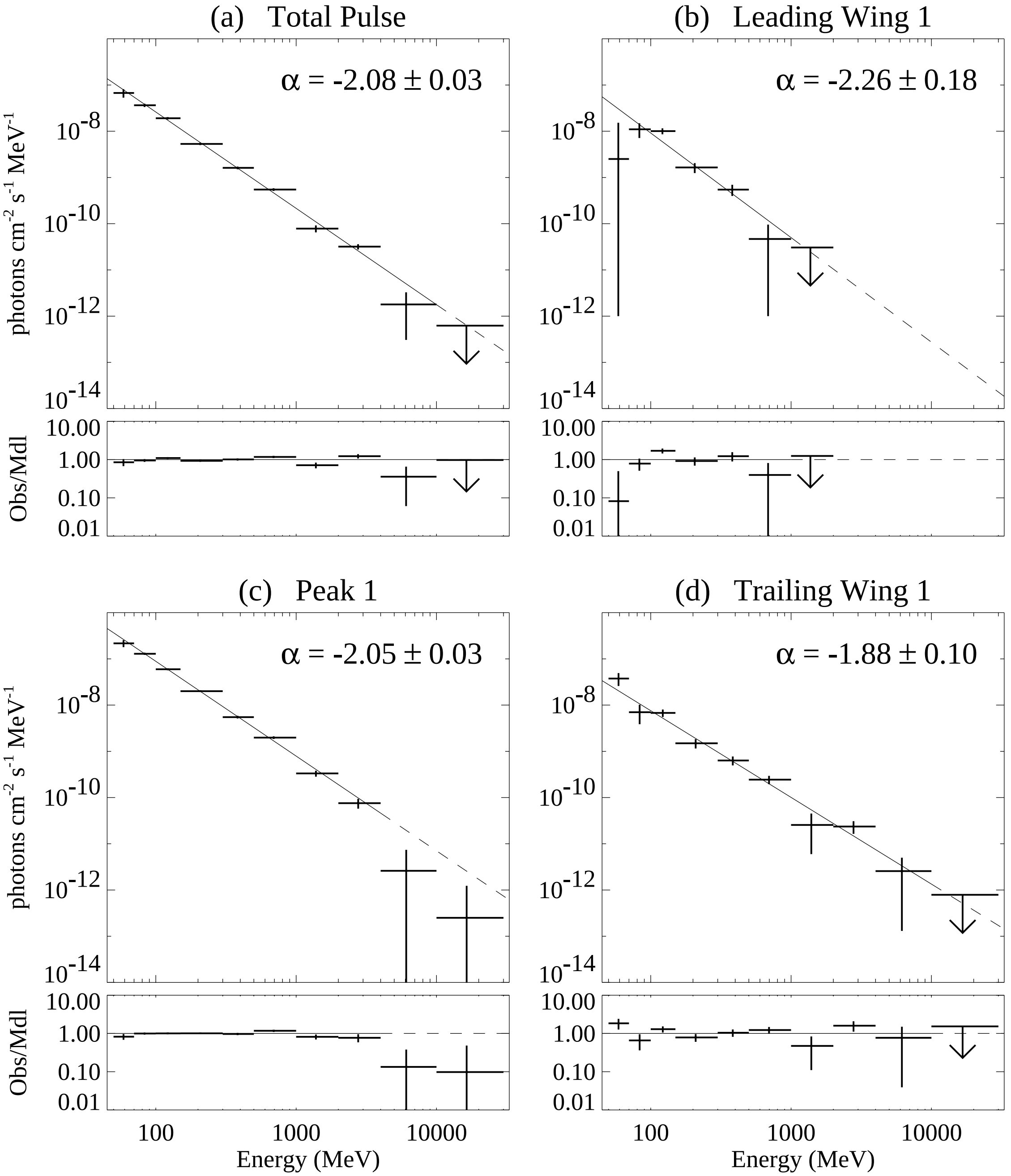

Figure 5.15: Differential photon spectra derived from pulsed analysis of the Crab (a) total pulse, and first pulse (b) leading wing, (c) peak, and (d) trailing wing components. The upper limits are 2σ.

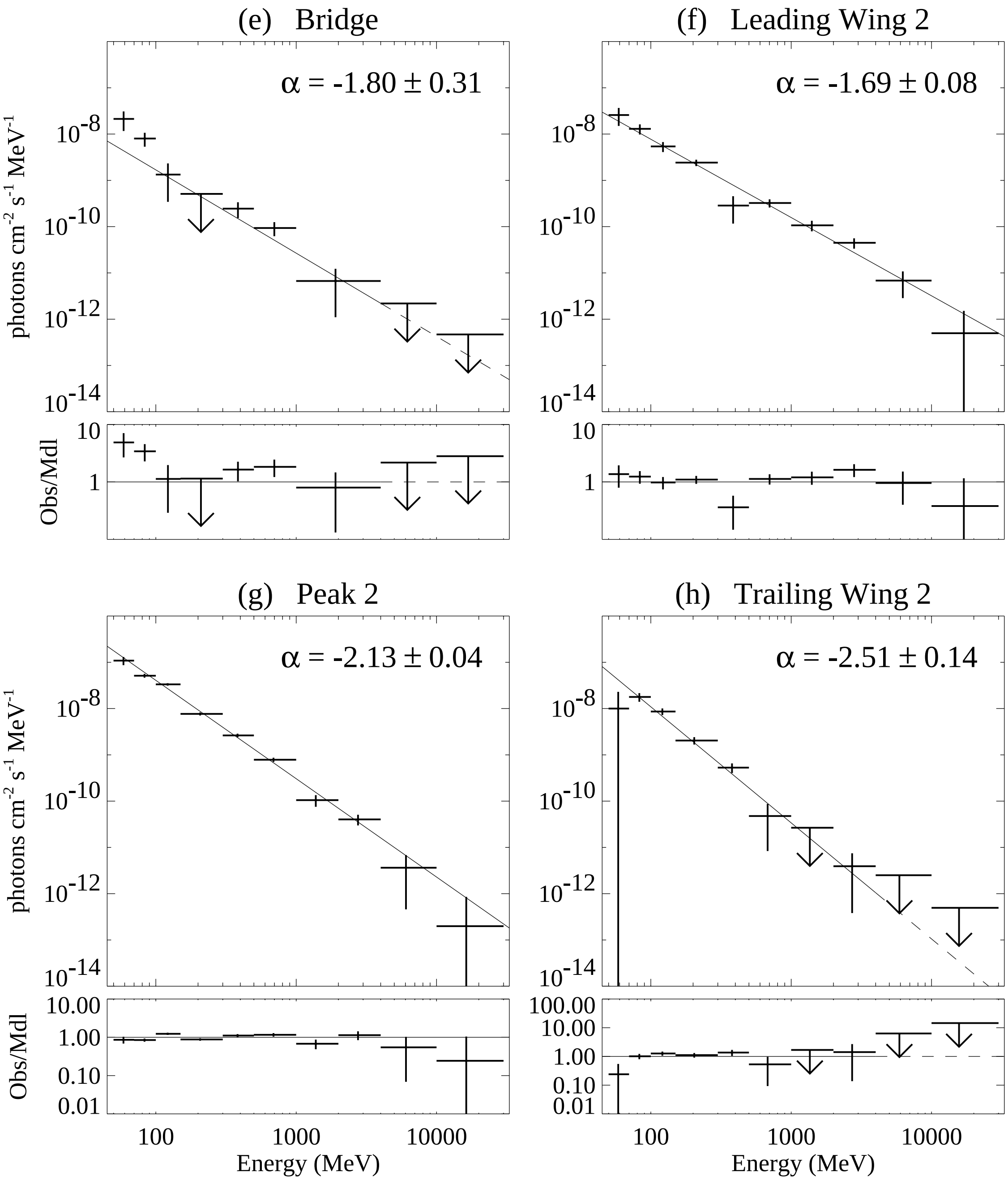

Figure 5.15: (continued) Differential photon spectra derived from pulsed analysis of the Crab (e) bridge, and second pulse (f) leading wing, (g) peak, and (h) trailing wing components. The upper limits are 2σ.

emission in the offpulse region does not result in a deficiency of counts at low energies in the other components, providing further evidence that the ultra-soft emission is present at the same level throughout the pulse profile. Even though the high-energy emission from the OP is also subtracted, positive detections of emission from the LW2 and P2 components were made in the highest energy bins, implying that Crab is emitting is pulsed radiation out to ~ 30 GeV.

5.6 Giant Pulses

The multiwavelength alignment of the Crab pulse profile essentially requires that the pulsed emission from radio to γ-ray energies originates from the same areas of the pulsar magnetosphere. The Crab pulsar is known to emit extremely intense single pulses at radio frequencies (Heiles, Campbell, & Rankin 1970; Staelin & Sutton 1970). In fact, the original radio discovery of the pulsar (Staelin & Reifenstein 1968) was made possible through the detection of these *giant pulses*. If the giant pulses are due to momentary increases in the general production of photons, a similar effect should be seen at higher energies coincident with the giant radio pulses. In a study of the giant pulse phenomenology, Lundgren et al. (1995) performed radio observations from 1991 May 15–27 with the Greenbank 43 m telescope, using linearly polarized feed antennas at 1330 MHz for two days, at 800 MHz for one day, and at 812.5 MHz for 10 days. Samples were taken in hour-long scans for a total of 10 hours per day, resulting in the detection of $\sim 28,000$ giant pulses during 10^7 pulsar rotation cycles. The observations were made concurrently with the *CGRO* observation VP 0010—during which the Crab was $6^\circ\!.4$ away from the instrument pointing axis—for the express purpose of searching for a correlation between increased radio and γ-ray emission.

To be classified as a giant pulse, an individual radio pulse had to be at least 10% of the Crab nebula's flux density and appear in two frequency bands with the correct dispersion offset. Roughly 90% of the giant pulses correspond to the main radio pulse. A histogram of the flux densities of the giant pulses detected at 812.5 MHz is shown in Figure 5.16. The great majority of radio pulsars have Gaussian or exponential pulse flux density distributions with a maximum pulse intensity of ~ 10 time the average (Hesse & Wielebinski 1974; Ritchings 1976), but the tail end of the Crab distribution behaves roughly as a power law with an index of -3.5 out to single pulses which are ~ 2000 times brighter than the average main pulse. The sharp cutoff at ~ 120 Jy in Figure 5.16 is due to the selection criteria for a giant pulse. The rollover at ~ 200 Jy is apparently real, and indicates a cutoff in the giant pulse power law distribution below intensities ~ 33 times the average weak pulse intensity (Lundgren et al. 1995).

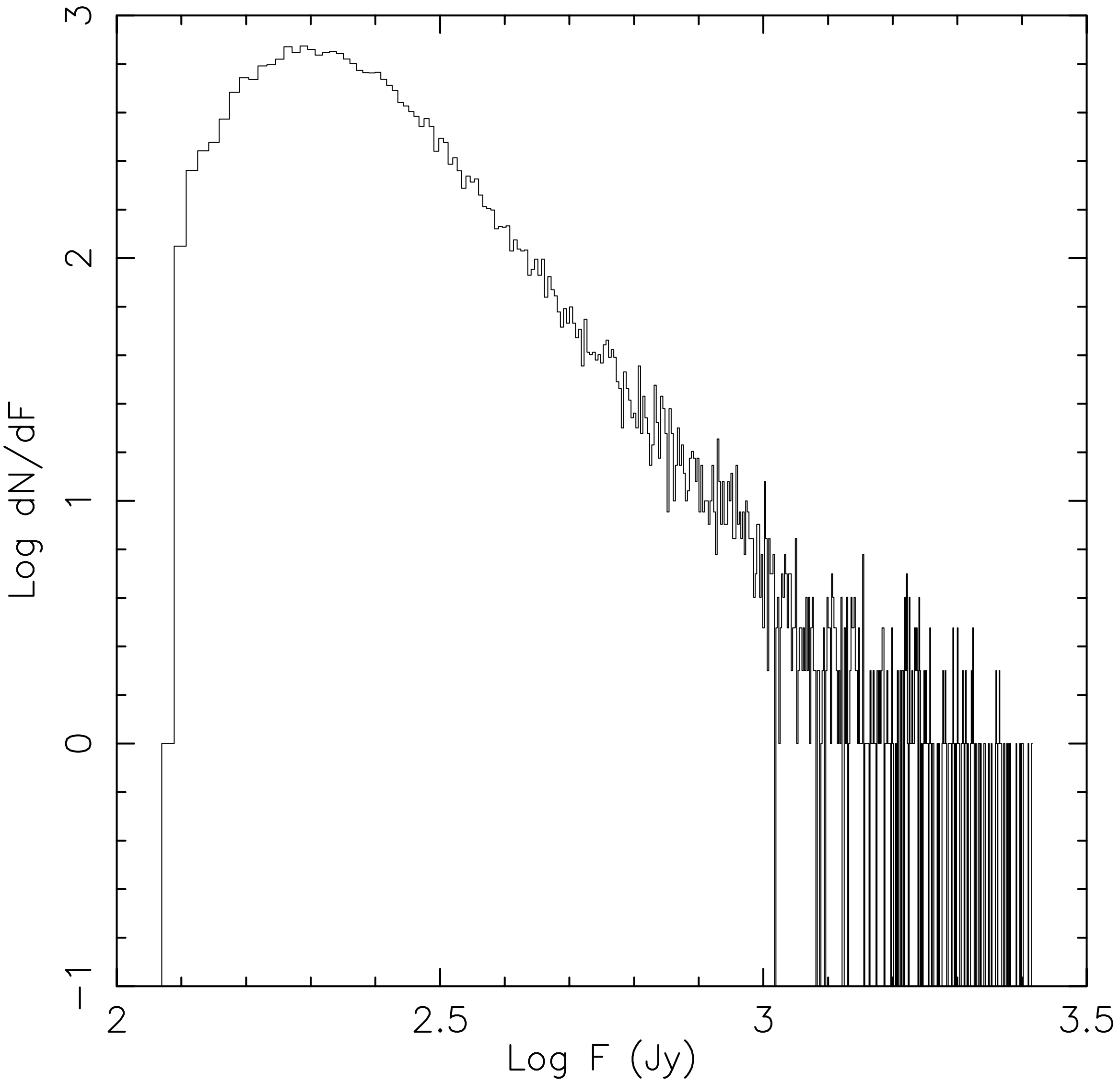

Figure 5.16: Histogram of Crab giant pulse flux densities. The logarithms are base 10. The tail end behaves as a power law with an index of −3.5. The average Crab pulse intensity is 2–3 Jy. Reprinted from Lundgren et al. (1995).

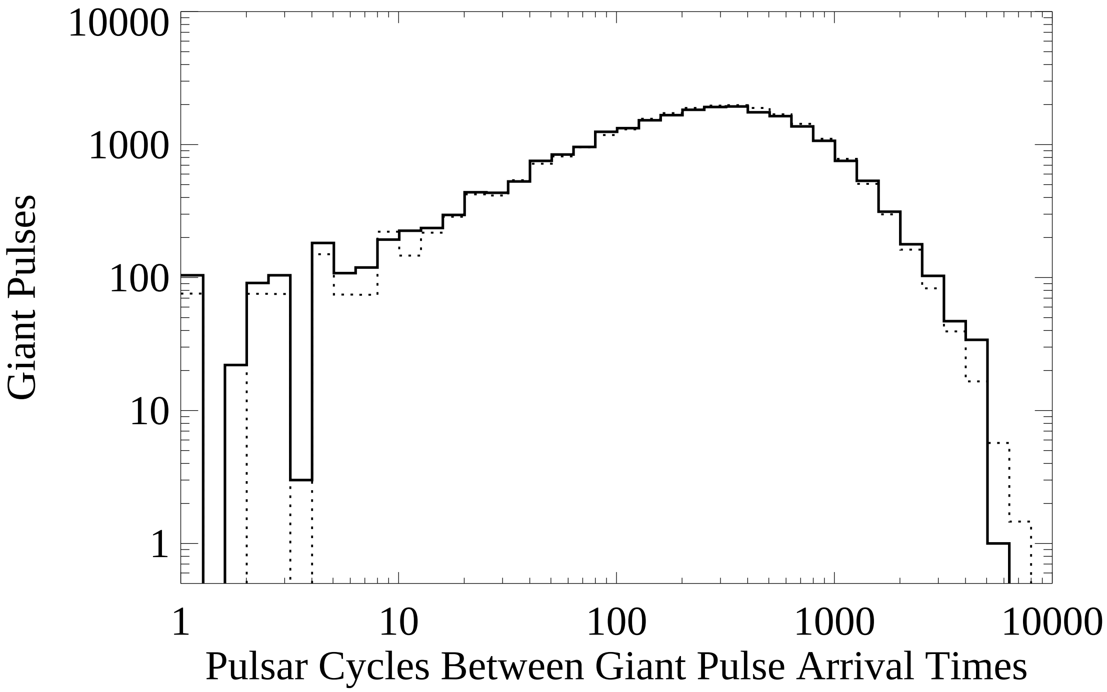

Figure 5.17: Histogram of the time separation between Crab giant pulse arrival times. The time is plotted in units of the Crab pulsar rotation period. The dotted line is the distribution expected from a purely Poisson process.

The arrival times of the giant pulses were converted to barycentric time with an accuracy of 70 μs. If the giant pulses are independent of one another, the time from one giant pulse to the next should be distributed according to the Poisson process probability

$$p(\Delta T)\, d\Delta T = \lambda\, e^{-\Delta T/\lambda}\, d\Delta T \ , \tag{5.9}$$

where ΔT is the separation time and λ is the average separation time. The distribution expected from a Poisson process is plotted together with the measured distribution of giant pulse separation times in Figure 5.17. The modeled distribution has taken into account that the separation times are not a continuous function, but, rather, they are sampled at discrete intervals determined by the pulsar period. The distribution is well-described by the Poisson process, indicating that the giant pulses occur independently of one another.

It would now seem a straightforward matter to look for increased γ-ray emission coincident with the detection of a giant pulse. To optimize the signal-to-noise, only γ-rays of energy greater than 100 MeV and arriving within an angle θ_{67} from the radio position of the

Crab pulsar are selected, with θ_{67} defined in equation (3.1). During the thirteen days of 10 hour radio observations, roughly 28,000 giant pulses were detected, or approximately one giant pulse every 500 rotations. In contrast, *EGRET* detected only 1470 γ-rays satisfying the selection criteria over the course of the 14-day observation VP 0010. Even accounting for extended periods of instrument dead time, a high-energy γ-ray arriving within the acceptance cone was only measured once every $\sim$ 9,000 pulsar rotations. Thus, instead of searching for increased γ-ray emission coincident with Crab giant pulses, it is more practical to search for *any* γ-ray emission near the occurrence of a giant pulse.

Suppose that the Crab pulsar is simultaneously monitored by radio and γ-ray telescopes for a period of time T. For uncorrelated γ-ray and giant pulse emission, the expected number of γ-rays coincident with giant pulse emission is

$$\mu = \frac{N_{\mathrm{GIANT}}\,\Delta t}{T} \times N_\gamma \ , \tag{5.10}$$

where N_γ is the total number of γ-rays detected by *EGRET*, N_{GIANT} is the number of giant pulses recorded during the same period, and Δt is the window of time around each giant pulse used to search for a coincident γ-ray. From Poisson statistics, the probability that N or more γ-rays will be detected coincident with a giant radio pulse is

$$P(\geq N|\mu) = \sum_{i=N}^{\infty} \frac{\mu^i e^{-\mu}}{i!}. \tag{5.11}$$

In the event that no evidence is found of a correlation between γ-rays and giant pulses, it is important to establish an upper limit on the factor f by which the γ-ray emission increases during giant pulse emission times. Using a likelihood ratio test (Hearn 1969), the upper limit on f is found by solving

$$1 - C = \frac{P(f\mu|N)}{P(\mu|N)} \ , \tag{5.12}$$

where C is the desired confidence level and $P(\mu|N)$ is the probability that there is a true average number of coincident counts μ given the N measured coincident counts. Following Bayes' Theorem, this ratio can be expressed as

$$\frac{P(f\mu|N)}{P(\mu|N)} = \frac{P(f\mu)P(N|f\mu)}{P(\mu)P(N|\mu)} \ , \tag{5.13}$$

where $P(\mu)$ is the a priori probability of having μ coincident counts. Since the basis of this study is that there is no knowledge of the level of increase in γ-ray emission, the assumption

Table 5.9: γ-Rays Within Five Periods of a Crab Giant Pulse

Component	T (days)	N_{GIANT}	N_γ	Coincidences Pred	Meas	Prob	f (95%)
Peak 1	3.49	24,488	107	2.90	5	17%	4.7
Peak 2	3.64	2,922	65	0.20	0	100%	15.9
Total Pulse	3.58	27,390	327	9.68	11	38%	2.2

here is that $P(\mu) = P(f\mu)$. Thus, the 95% upper limit on f is obtained by solving

$$0.05 = \frac{P(N|f\mu)}{P(N|\mu)} = e^{\mu(1-f)} f^N \ . \tag{5.14}$$

The results of the analysis are presented in Table 5.9. Here, a coincidence is arbitrarily defined as a γ-ray which arrives within five rotation cycles of a giant pulse. Identical studies were also performed for coincidence definitions ranging from 1–50 rotation cycles. For the first peak analysis, only the main peak giant pulses and γ-rays falling within the P1 phase interval are considered. Likewise, the second peak analysis uses only the second peak giant pulses and γ-rays from the P2 component. For the total pulse analysis, all recorded giant pulses and γ-rays matching the selection criteria are considered. The effective observation time T is calculated by determining when the Crab pulsar was observable to both the radio observatory and *EGRET*. Since the Greenbank telescope observations were made for only 10 hours per day, and the Crab pulsar was obscured behind the Earth during a large portion of each *CGRO* orbit, T is much less than the 13 days of simultaneous observations. Anomalously long time spans between giant pulses is a possible indication that adjustments were being made to the radio telescope at that time, and these dead times are excluded from the analysis. Since the rate of measured giant pulses from the second peak is $\sim 1/8$ the rate measured from the the first peak, extended dead times are not as easy to identify, so fewer dead times are excluded for the peak 2 data set than for the peak 1 data set. For the total pulse data set, the same threshold was used to detect dead times as was employed for the peak 1 data set. Since the total data set has more giant pulses than the peak 1 data set, there will be fewer apparent dead times.

There is no evidence of an increase in γ-ray emission coincident with the arrival of a giant pulse. For the total pulse profile, a 95% upper limit to the factor by which the emission increases is $f \leq 2.2$. Varying the coincidence definition and phase intervals produced comparable results. The giant pulses used in this study have intensities from 100–2000 times the average radio pulse intensity, but no comparable effect is observed above 100 MeV. The 11 coincident γ-rays found for the total pulse analysis have no special properties, with only

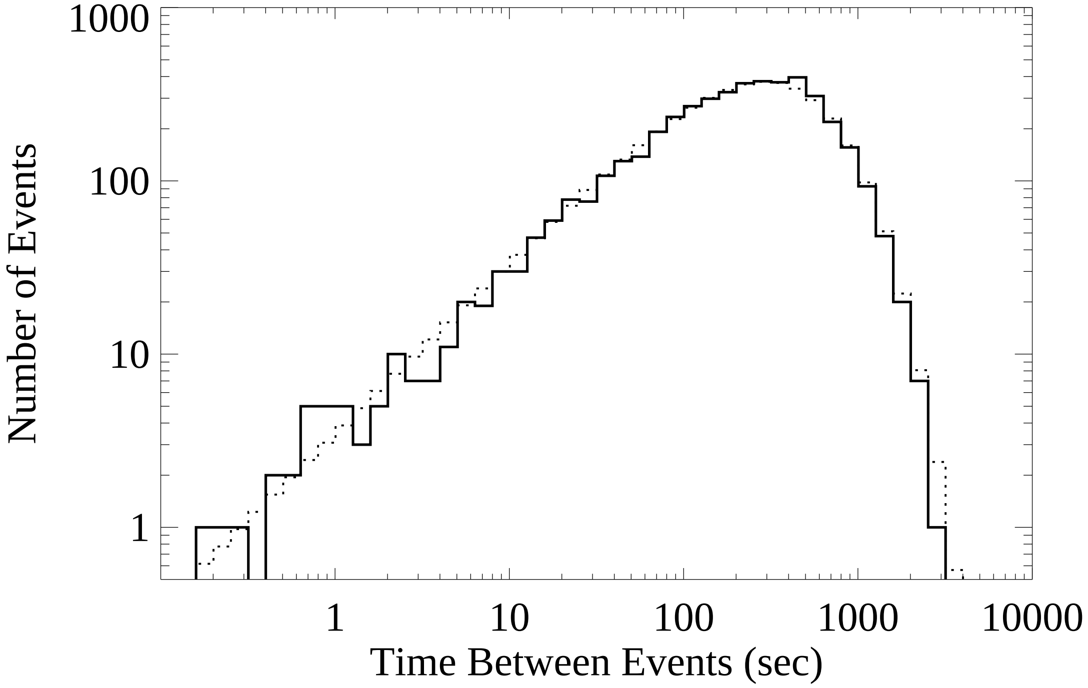

Figure 5.18: Histogram of the time separation between Crab γ-ray arrival times. The dotted line is the distribution expected from a purely Poisson process.

one of the photons detected with an energy above 250 MeV

5.7 Pulse Nulling

Although pulsars have shown steady long-term radio emission, a few radio pulsars exhibit short-term variations in the form of *pulse nulling* (Ritchings 1976), during which no emission is detected from the pulsar for many consecutive periods. While this behavior has not been detected from the Crab radio pulsar, it is possible that such short-term variations are occurring in the *EGRET* energy range.

Photon events were selected from an energy-dependent cone θ_{67} about the radio pulsar position, and were required to have a measured energy greater than 100 MeV. The instrument detection efficiency is known to vary depending on the quality of the gas in the spark chamber, so it is expected that the rate of photons detected from the Crab will also vary from observation to observation. A distribution of the separation times between γ-ray events was recorded for each observation. Using the average time between events for each observation, a distribution due to purely Poisson process was also generated. The measured and predicted distributions were then added for all observations in Table 5.1, and the results are shown in Figure 5.18. The agreement between the distributions is extremely good, with a χ^2 value of 31.4 for 42 degrees of freedom. Distributions were also formed using only the P1 and P2 components of the pulse profile, and in each case the resulting distribution is consistent with a Poisson process. If there were extended gaps in the emission from the Crab, or if there were periods of sudden increase in the rate of emission, it would cause the measured distribution to deviate from the predicted distribution. From Figure 5.18, it can be concluded there is no significant short-term variation in the rate of γ-ray emission from the Crab pulsar.

5.8 Discussion

The *EGRET* observations of the Crab complex have confirmed and expanded upon many of the results derived from *SAS 2* and *COS B* observations. As expected, two peaks dominate the γ-ray lightcurve, and are essentially coincident with their radio frequency counterparts, with the first peak measuring an offset of -0.01 ± 0.03 in phase. Both peaks appear to have extended tails of emission, particularly in the trailing wings. Surprisingly, the bridge emission between the two peaks, which has historically been assumed to be well above the baseline emission, drops off to a level which is consistent with the weakest level of emission in the pulse profile. Since the nebular contribution cannot be greater than this flux level, unpulsed emission accounts for no more than $12\% \pm 6\%$ of the total Crab emission above 100 MeV. There is no evidence of either long-term or short-term variability in the Crab total emission, spectral behavior, or pulse profile. In particular, the *EGRET* observations do not show any significant variation in the ratio of the strength of the second peak to that of the first. However, the results do not conflict with the possible long-term sinusoidal variation in the P2/P1 ratio suggested by Kanbach (1990).

Likelihood analysis of the spatial distribution of γ-rays has shown that there is emission above the diffuse background emission throughout the pulse profile, and that the level of emission and spectral characteristics vary dramatically as a function of pulsar phase. A phase-resolved study reveals that the hardness ratio defined in equation (5.7) rises smoothly through the first peak, and drops off gradually through the second peak. While the total emission from the Crab is well fit above 100 MeV by a single power low of spectral index -2.12 ± 0.03, the spectral indices from the individual components range from -1.6 to -2.6. There is no indication of a high-energy cutoff in any of the components, although the P1 component does show marginal evidence of a slight rollover. The four weakest pulsar components are dominated by ultra-soft emission at energies below $\sim$100 MeV. Double power law fits to the photon spectra from these four components show that the soft emission has an average spectral index of -4.4 ± 0.3 and a flux of $(1.1 \pm 0.2) \times 10^{-8}$ photons cm^{-2} s^{-1} MeV^{-1}at 100 MeV. This ultra-soft component is also apparent in a double power law fit to the total Crab emission. If the excess emission in the offpulse region is due solely to nebular emission, then a pulsed analysis relative to this component will isolate the modulated contribution. However, power law fits to the resulting spectra are unacceptable, perhaps indicating the presence of magnetospheric emission in the offpulse component. Subtracting the ultra-soft, low-energy emission present in the offpulse region from the rest of the components in the pulsed analysis does not lead to a strong break from power law behavior at low energies, further evidence of an unpulsed steep-spectrum component in the Crab γ-ray emission.

It would not be unreasonable to expect ultra-soft nebular emission out to energies on the order of $\sim$ 100 MeV. The emission at X-ray and soft γ-ray energies is consistent with synchrotron radiation produced by relativistic electrons streaming from the pulsar (Kennel & Coroniti 1984). Since the Crab pulsar is unlikely to produce electrons with energies greater than $\sim 10^{15}$–10^{16} eV, the synchrotron spectrum will begin to rollover at energies above a few MeV. The soft emission observed from 30–100 MeV is then seen as the tail end of the synchrotron emission from the nebula. The detection of unpulsed emission from the Crab complex at TeV energies (Weekes et al. 1989) implies that there is emission from the nebula beyond the synchrotron radiation. The TeV emission is explainable in terms of inverse-Compton scattering (de Jager & Harding 1992), which has also been proposed as a possible explanation of the harder-spectrum, high-energy offpulse emission. However, based on the level of the TeV emission, the expected inverse-Compton contribution at energies on the order of $\sim$1 GeV is below the *EGRET* flux measurements (Aharonian & Atoyan 1995). Perhaps, then, pulsed radiation is responsible for much of the offpulse emission, and, in particular, the harder power-law emission shown in Figure 5.14d which is dominant at higher energies.

If the ultra-soft component represents the extent of the nebular contribution to the total Crab emission, then above 100 MeV the nebular emission is negligible and equation (5.1) is an accurate description of the pulsar emission. This implies that the energy flux S_γ from 100 MeV to 10 GeV is

$$S_\gamma = \int_{100\ \mathrm{MeV}}^{10\ \mathrm{GeV}} E\,\frac{dN}{dE}\,dE = (1.49 \pm 0.05) \times 10^{-9}\ \mathrm{ergs\ cm^{-2}\ sec^{-1}}\ . \tag{5.15}$$

The γ-ray luminosity of the pulsar is defined as

$$L_\gamma = S_\gamma\,\Delta\Omega\,D^2\ , \tag{5.16}$$

where $\Delta\Omega$ is the effective solid angle into which the pulsar radiation is beamed and D is the distance to the pulsar. There is a great deal of uncertainty regarding these two quantities. From kinematic studies of the Crab nebular expansion, the distance to the Crab pulsar is estimated to be 2.0 ± 0.5 kpc (Taylor & Cordes 1993). The beaming angle has an even greater relative uncertainty. Since the pulsed emission is spread across much of the rotation phase, the beaming angle cannot be too narrow. But since the pulse does show some modulation, the emission must be beamed. Beyond these two general considerations, the opinions regarding the beaming angle are as diverse as the models. Rather than making unjustifiable assumptions, the beaming angles in this thesis are uniformly set to $\Delta\Omega = 1.0$ sr for all pulsars. This value is chosen more for simplicity than based on physical considerations. This leads to an inferred luminosity for the Crab pulsar between 100 MeV and 10 GeV of $L_\gamma = (5.7 \pm 2.8) \times 10^{34}$ ergs s^{-1}. From equation (2.2), the total spin-down power of the Crab pulsar is $\dot{E} = 4.5 \times 10^{38}$ ergs s^{-1}. Hence, the Crab is converting $\eta_\gamma \equiv L_\gamma/\dot{E} = (1.3 \pm 0.6) \times 10^{-4}$ of its available spin-down power into high-energy γ-rays. In comparison, the Crab pulsar emits $\sim 10^{36}$ ergs s^{-1} over the X-ray energy range of 0.1–4.5 keV (Harnden & Seward 1984). So the high-energy γ-ray emission detected from the Crab pulsar is a small fraction of the total power observed over the electromagnetic spectrum.

The lack of a strong spectral turnover in the Crab pulsar emission would seem to indicate that the modulated γ-rays are coming from far out in the pulsar magnetosphere. It is almost inconceivable that photons of energy ~ 10 GeV produced near the stellar surface would not be heavily attenuated when crossing the dipolar field lines associated with the 3.8×10^{12} G surface magnetic field. Only if the rotation and magnetic axes were nearly parallel and pointing towards Earth could the surface photons avoid crossing field lines with a sizeable perpendicular component and still be detectable by *EGRET*. This contradicts the long-held assumption that the Crab rotation and dipole axes are nearly orthogonal, a condition that can also explain the double-peaked profile. Still, the fact that the pulse profile has almost identical features from radio to γ-ray wavelengths requires that the emission at all energies originate from the same areas in the magnetosphere. It is difficult to explain the coherent radio emission without employing a pair production cascade, which requires a strong magnetic field. Yet, if the field is too strong, there should be a greater attenuation of high-energy photons. One clue to this mystery may come from the giant pulse analysis, which shows that there is no correlation between radio frequency giant pulses and increased γ-ray emission. This indicates that the giant pulses do not result from an enhancement in the same pair-production process that creates the γ-rays, but instead an enhancement in the radio coherence mechanism.